Finite-element-based computational methods for cardiovascular fluid-structure interaction

F.N. VAN DE VOSSE[1], J. DE HART[1], C.H.G.A. VAN OIJEN[1], D. BESSEMS[1],
T.W.M. GUNTHER[1], A. SEGAL[2], B.J.B.M. WOLTERS[1], J.M.A. STIJNEN[1] and
F.P.T. BAAIJENS[1]
[1]*Eindhoven University of Technology, Department of Biomedical Engineering, P.O. Box 513, 5600 MB, Eindhoven, The Netherlands;* [2]*Delft University of Technology, Department of Mathematics and Computer Sciences, P.O. Box 513, 5600 MB, Eindhoven, The Netherlands*

Abstract. In this paper a combined arbitrary Lagrange-Euler fictitious domain (ALE-FD) method for fluid-structure interaction problems in cardiovascular biomechanics is derived in terms of a weighted residual finite-element formulation. For both fluid flow of blood and solid mechanics of vascular tissue, the performance of tetrahedral and hexahedral Crouzeix-Raviart elements are evaluated. Comparable convergence results are found, although for the test cases considered the hexahedral elements are more accurate. The possibilities that are offered by the ALE-FD method are illustrated by means of a simulation of valve dynamics in a simplified left ventricular flow model.

Key words: arbitrary Lagrange-Euler, blood flow, fictitious domain, fluid-structure interaction, vascular-tissue mechanics

1. Introduction

In cardiovascular biomechanics one of the major topics today is the simulation and analysis of the hemodynamics of the cardiovascular system using computational methods [1]. Because of its flexible nature and the prospect of modeling fluid-structure interaction (FSI) between blood flow and vessel wall deformation, these computational methods are often based on the finite-element method (FEM). When looking at the future, patient-specific models are going to be used to improve on-line model-based diagnostics and evaluate alternatives in surgical planning of cardiovascular disease. These applications demand fast computations using detailed geometries obtained from X-ray angiography, computed tomography (CT), ultrasound (US) and magnetic resonance imaging (MRI).

As the dimensions of arteries change with the varying internal blood pressure, both fluid flow and solid deformation are involved. In order to incorporate this fluid-structure interaction in a mathematical model, a classical Galerkin finite-element method can be used to approximate the solution of the Navier-Stokes equations for fluid flow and the balance equations for solid deformation. Within this finite-element framework, the rheological behavior of blood [2, 3] and the nonlinear constitutive behavior of biological tissue [4] can be incorporated in a mathematically founded way. Besides the complex constitutive behavior, in cardiovascular biomechanics the geometry of the domains can be very complex. Nowadays two basic element shapes are most commonly used for three-dimensional analysis of fluid flow and solid mechanics, namely hexahedral and tetrahedral elements. Both shapes have their own advantages

and disadvantages [5, 6]. Apart from accuracy and stability considerations, the main advantage of tetrahedra is that powerful mesh-generators are available to triangulate complex domains.

An arbitrary Lagrange-Euler (ALE) method originating from the modeling of metal-forming processes [7, 8] can be used to accommodate for the deformation of the fluid domain surrounded by a moving/deforming solid [9] and have been used for fluid-structure interaction problems in vascular systems in the past [10–12]. A more complicated interaction model is needed to describe the movement of solid structures that are immersed in the fluid. This coupling can be realized by a set of dynamic and kinematic constraints that are enforced through Lagrange multipliers [13–15]. Successful application of this so-called fictitious domain method that actually originates from Peskin's immersed boundary technique [16] and is combined with an ALE method can be found in [17–19].

The objective of this paper is to illustrate the potential of a combined arbitrary Lagrange-Euler fictitious-domain (ALE-FD) method for cardiovascular fluid-structure interaction and to indicate how this method can make use of the latest developments in finite-element modeling of blood flow and biological tissue mechanics. Hereto, in Section 2 an alternative derivation of the fictitious domain method, not based on Lagrange multipliers but in the context of a weak formulation of the governing equations will be given. Next in Section 3 some remarks on admissible finite element spaces are made. Numerical tests in Section 4 will provide information on the applicability of hexahedral and tetrahedral elements. Some examples of fluid-structure interaction problems that arise in cardiovascular biomechanics will be given in Section 5. Finally a summary of conclusions will be discussed in Section 6.

2. Governing equations

2.1. FLUID MOTION

2.1.1. *Conservation of mass and momentum*
Introducing v as the fluid velocity, we can write the momentum equation for a fluid with density ρ in domain $\Omega \subset \mathbb{R}^3$ with boundary Γ as

$$\rho \frac{\partial v}{\partial t} + \rho(v \cdot \nabla v) = \nabla \cdot \sigma + f \qquad \text{in } \Omega, \tag{1}$$

where t denotes the time, σ the Cauchy stress tensor and f the body forces per unit of volume. If incompressibility of the fluid is assumed, conservation of mass reduces to the continuity equation

$$\nabla \cdot v = 0 \qquad \text{in } \Omega. \tag{2}$$

The Cauchy stress tensor σ is written in terms of the hydrostatic pressure p and the extra stress tensor τ, *i.e.*:

$$\sigma = -p\mathbf{I} + \tau. \tag{3}$$

The pressure in (3) can be seen as a Lagrange multiplier to enforce the incompressibility constraint (2) and, together with appropriate boundary and initial conditions and a constitutive equation that expresses the material properties of the fluid, a unique solution of the set of differential equations (1) and (2) in terms of the unknown pressure p and velocity v can be found [20, Chapter 2].

2.1.2. *Boundary and initial conditions*

For each part Γ_k of the boundary $\Gamma = \bigcup_k \Gamma_k$ with $\forall_{k \neq l} \; \Gamma_k \cap \Gamma_l = \emptyset$, outer normal $\boldsymbol{n}$ and tangential directions $\boldsymbol{t_1}$ and $\boldsymbol{t_2}$, the boundary conditions are as follows:

$$\boldsymbol{v} \cdot \boldsymbol{n} = v_n \quad \vee \quad (\boldsymbol{\sigma} \cdot \boldsymbol{n}) \cdot \boldsymbol{n} = s_n$$
$$\text{in } \Gamma_k \qquad (4)$$
$$\boldsymbol{v} \cdot \boldsymbol{t_i} = v_{t_i} \quad \vee \quad (\boldsymbol{\sigma} \cdot \boldsymbol{n}) \cdot \boldsymbol{t_i} = s_{t_i}, \qquad i = 1, 2$$

where, in the case of Dirichlet conditions, v_n and v_{t_i} denote the prescribed normal and tangential components of the velocity vector $\boldsymbol{v}$ and, in the case of Neumann conditions, s_n and s_{t_i} denote the prescribed normal and tangential components of the stress vector $\boldsymbol{s} = \boldsymbol{\sigma} \cdot \boldsymbol{n}$. Note that boundary conditions are given in terms of components of the velocity and stress vector. As a consequence, only for fully developed outflow velocity boundary a prescribed normal component of the stress vector, together with zero tangential velocity corresponds with a prescribed pressure. Initial conditions must be given for the velocity, *i.e.*, $\boldsymbol{v}|_{t=0} = \boldsymbol{v}^0$ and, depending on the time integration that will be used, for the pressure $p|_{t=0} = p^0$.

2.1.3. *Constitutive equations*

If an inelastic generalized Newtonian flow behavior is assumed, the Cauchy stress tensor $\boldsymbol{\sigma}$ can be written as

$$\boldsymbol{\sigma} = -p\mathbf{I} + 2\eta(\dot{\gamma})\mathbf{D}_v, \qquad (5)$$

where $\eta(\dot{\gamma})$ is the shear-rate-dependent dynamic viscosity and $\mathbf{D}_v$ denotes the rate of deformation tensor

$$\mathbf{D}_v = \frac{1}{2}[\nabla \boldsymbol{v} + (\nabla \boldsymbol{v})^T]. \qquad (6)$$

The shear-rate parameter $\dot{\gamma}$ must be defined in terms of the second invariant of the rate of deformation tensor $\mathbf{D}_v$. For incompressible fluids this is

$$\dot{\gamma} = \sqrt{2\mathbf{D}_v : \mathbf{D}_v}. \qquad (7)$$

In [2, 3] it is shown that the non-Newtonian behavior of blood can be described very well with the Carreau-Yasuda model:

$$\frac{\eta(\dot{\gamma}) - \eta_\infty}{\eta_0 - \eta_\infty} = [1 + (\lambda\dot{\gamma})^a]^{\frac{n-1}{a}} \qquad (8)$$

with η_0, η_∞, λ, a and n being parameters of the model. For a time constant $\lambda = 0$ this model reduces to a simple Newtonian model with $\eta(\dot{\gamma}) = \eta_0$.

2.1.4. *Weak form*

If we define $\boldsymbol{W} = \{\boldsymbol{w} \in [H_0^1(\Omega)]^3\}$ with $H_0^1(\Omega)$, the Hilbert space satisfying the homogeneous version of the Dirichlet boundary conditions given in (4) and $Q = \{q \in L^2(\Omega); \int_\Omega q \mathrm{d}\Omega = 0\}$, the weak formulation of (1) and (2) after partial integration and substitution of the Neumann

boundary conditions is:

$$\int_\Omega \boldsymbol{w} \cdot \rho \left(\frac{\partial \boldsymbol{v}}{\partial t} + \boldsymbol{v} \cdot \nabla \boldsymbol{v} \right) \, \mathrm{d}\Omega + \int_\Omega (\nabla \boldsymbol{w})^T : \boldsymbol{\tau} \, \mathrm{d}\Omega - \int_\Omega p \nabla \cdot \boldsymbol{w} \, \mathrm{d}\Omega =$$

$$= \int_\Omega \boldsymbol{w} \cdot \boldsymbol{f} \, \mathrm{d}\Omega + \int_\Gamma \boldsymbol{w} \cdot \boldsymbol{s} \, \mathrm{d}\Gamma \qquad \forall \boldsymbol{w} \in \boldsymbol{W}, \qquad (9)$$

$$\int_\Omega q \nabla \cdot \boldsymbol{v} \, \mathrm{d}\Omega = 0 \qquad \forall q \in Q,$$

with in our case $\boldsymbol{\tau} = 2\eta(\dot{\gamma})\mathbf{D}$, although any other inelastic constitutive model can be used.

2.1.5. *Time integration*
If an implicit, backward-Euler, time integration is applied, one can write

$$\frac{\partial \boldsymbol{v}}{\partial t} \approx \frac{\boldsymbol{v} - \boldsymbol{v}^n}{\Delta t}, \qquad (10)$$

where $\boldsymbol{v} = \boldsymbol{v}^{n+1}$ is the unknown velocity at t^{n+1} and $\boldsymbol{v}^n$ is the known velocity at t^n with $\Delta t = t^{n+1} - t^n$. The vector $\boldsymbol{v}^0$ must be defined by the initial condition for the velocity.

2.1.6. *Linearization*
Linearization of the nonlinear convective term $\boldsymbol{v} \cdot \nabla \boldsymbol{v}$ can be carried out with a Newton iteration process. Let $\boldsymbol{v}$ be the converged solution and $\hat{\boldsymbol{v}}$ an estimate of this solution. Then the variation $\delta \boldsymbol{v}$ can be defined as $\delta \boldsymbol{v} = \boldsymbol{v} - \hat{\boldsymbol{v}}$. Elaboration on the convective term yields

$$\left(\hat{\boldsymbol{v}} + \delta \boldsymbol{v} \right) \cdot \nabla \left(\hat{\boldsymbol{v}} + \delta \boldsymbol{v} \right) = \hat{\boldsymbol{v}} \cdot \nabla \hat{\boldsymbol{v}} + \hat{\boldsymbol{v}} \cdot \nabla \delta \boldsymbol{v} + \delta \boldsymbol{v} \cdot \nabla \hat{\boldsymbol{v}}, \qquad (11)$$

where higher-order terms in $\delta \boldsymbol{v}$ are neglected. As the extra stress $\boldsymbol{\tau}$ also depends on $\boldsymbol{v}$, it must also be expressed in terms of its estimate $\hat{\boldsymbol{\tau}}$ and variation $\delta \boldsymbol{\tau}$. The following linearized set of equations is obtained:

$$\int_\Omega \boldsymbol{w} \cdot \rho \left(\frac{\delta \boldsymbol{v}}{\Delta t} + \hat{\boldsymbol{v}} \cdot \nabla \delta \boldsymbol{v} + \delta \boldsymbol{v} \cdot \nabla \hat{\boldsymbol{v}} \right) \, \mathrm{d}\Omega + \int_\Omega (\nabla \boldsymbol{w})^T : \delta \boldsymbol{\tau} \, \mathrm{d}\Omega +$$

$$- \int_\Omega \delta p \nabla \cdot \boldsymbol{w} \, \mathrm{d}\Omega = \int_\Omega \boldsymbol{w} \cdot \boldsymbol{f} \, \mathrm{d}\Omega + \int_\Gamma \boldsymbol{w} \cdot \boldsymbol{s} \, \mathrm{d}\Gamma + \hat{r} \qquad \forall \boldsymbol{w} \in \boldsymbol{W}, \qquad (12)$$

$$\int_\Omega q \nabla \cdot \delta \boldsymbol{v} \, \mathrm{d}\Omega = - \int_\Omega q \nabla \cdot \hat{\boldsymbol{v}} \, \mathrm{d}\Omega \qquad \forall q \in Q,$$

with $p = \hat{p} + \delta p$. The residual $\hat{r}$, which only consists of known quantities, is defined by:

$$\hat{r} = \int_\Omega \left[\boldsymbol{w} \cdot \rho \left(\frac{\boldsymbol{v}^n - \hat{\boldsymbol{v}}}{\Delta t} - \hat{\boldsymbol{v}} \cdot \nabla \hat{\boldsymbol{v}} \right) - (\nabla \boldsymbol{w})^T : \hat{\boldsymbol{\tau}} + \hat{p} \nabla \cdot \boldsymbol{w} \right] \mathrm{d}\Omega. \qquad (13)$$

If we define $\mathbf{D}_a = \frac{1}{2}[\nabla \boldsymbol{a} + (\nabla \boldsymbol{a})^T]$, the extra stress $\boldsymbol{\tau}$ can be linearized according to:

$$\boldsymbol{\tau} = 2\eta(\dot{\gamma})\mathbf{D} = 2[\eta(\hat{\dot{\gamma}}) + \eta(\delta\dot{\gamma})](\mathbf{D}_{\hat{v}} + \mathbf{D}_{\delta v}) \approx 2\eta(\hat{\dot{\gamma}})\mathbf{D}_{\hat{v}} + 2\eta(\hat{\dot{\gamma}})\mathbf{D}_{\delta v} = \hat{\boldsymbol{\tau}} + \delta\boldsymbol{\tau}. \quad (14)$$

Note that in (14) the viscosity $\eta(\dot{\gamma})$ has been approximated by $\eta(\hat{\dot{\gamma}})$ based on the velocity of the previous iteration. As the viscosity only weakly depends on the shear rate, this successive substitution will result in a stable solution procedure in almost all practical cases. The weak formulation (12) will be taken as a point of departure for the finite-element method described in the Section 3.

2.2. SOLID DEFORMATION

2.2.1. *Conservation of mass and momentum*

The equation of motion and the continuity equation for an incompressible solid material defined in the domain $\Omega(t) \subset \mathbb{R}^3$ and bounded by $\Gamma(t)$ can be written as:

$$\nabla \cdot \boldsymbol{\sigma} = \boldsymbol{f} \qquad\qquad \text{in } \Omega(t),$$
$$\det(\mathbf{F}) - 1 = 0 \qquad\qquad \text{in } \Omega(t), \tag{15}$$

with $\boldsymbol{\sigma}$ the Cauchy stress tensor, $\boldsymbol{f}$ a body force per unit volume and $\mathbf{F} = (\nabla_0 \boldsymbol{x})^T$ the deformation-gradient tensor defining the deformation between reference state Ω_0 and the current configuration $\Omega(t)$. The Cauchy stress for an incompressible material again is written as

$$\boldsymbol{\sigma} = -p\mathbf{I} + \boldsymbol{\tau}, \tag{16}$$

where p is the hydrostatic pressure and $\boldsymbol{\tau}$ the extra stress resulting from deformation.

2.2.2. *Boundary conditions*

The set of equations is completed with a set of suitable boundary conditions at $\Gamma(t)$. The same as in the case of fluid flow, for each part Γ_k of the boundary $\Gamma = \bigcup_k \Gamma_k$ with $\forall_{k \neq l} \Gamma_k \cap \Gamma_l = \emptyset$, outer normal $\boldsymbol{n}$ and tangential directions $\boldsymbol{t_1}$ and $\boldsymbol{t_2}$, the boundary conditions can be of the form

$$\boldsymbol{x} \cdot \boldsymbol{n} = x_n \quad \vee \quad (\boldsymbol{\sigma} \cdot \boldsymbol{n}) \cdot \boldsymbol{n} = s_n$$
$$\qquad\qquad\qquad\qquad\qquad\qquad\qquad \text{on } \Gamma_k, \tag{17}$$
$$\boldsymbol{x} \cdot \boldsymbol{t_i} = x_{t_i} \quad \vee \quad (\boldsymbol{\sigma} \cdot \boldsymbol{n}) \cdot \boldsymbol{t_i} = s_{t_i}, \qquad i = 1, 2$$

where, in the case of Dirichlet conditions, x_n and x_{t_i} denote the prescribed normal and tangential components of the position vector $\boldsymbol{x}$ and, in the case of Neumann conditions, s_n and s_{t_i} denote the prescribed normal and tangential components of the surface-traction vector $\boldsymbol{s} = \boldsymbol{\sigma} \cdot \boldsymbol{n}$.

2.2.3. *Constitutive equations*

In order to describe the mechanical properties of cardiovascular tissue, various linear and non-linear constitutive equations for both isotropic and anisotropic material behavior, including or excluding residual strain, have been proposed. A review can be found in [21]. In this study we will consider a linear elastic neo-Hookean model and a fiber-reinforced arterial-wall model. For the neo-Hookean model, the extra stress is linear related to the Finger tensor. So:

$$\boldsymbol{\sigma} = -p\mathbf{I} + G(\mathbf{B} - \mathbf{I}), \tag{18}$$

with G the shear modulus and the Finger tensor $\mathbf{B}$ defined as:

$$\mathbf{B} = \mathbf{F} \cdot \mathbf{F}^T. \tag{19}$$

We will assume the shear modulus G to be constant although a scalar function of the invariants of $\mathbf{B}$ is also possible. For the arterial wall one can use a fiber-reinforced transversely isotropic material defined by an extra stress that is the sum of two contributions, a linear stress of the matrix $\boldsymbol{\tau}_m$ and a nonlinear fiber stress τ_f [4, 22]:

$$\boldsymbol{\sigma} = -p\mathbf{I} + \boldsymbol{\tau}_m + \tau_f \boldsymbol{e}\boldsymbol{e} \tag{20}$$

with

$$\boldsymbol{\tau}_m = G_m(\mathbf{B} - \mathbf{I}) \quad \text{and} \quad \tau_f = k_1 \lambda_f^2 (\lambda_f - 1) e^{k_2(\lambda_f^2 - 1)^2}. \tag{21}$$

Here G_m, k_1 and k_2 are the material parameters. The fiber stretch λ_f is defined by the deformation:

$$\lambda_f = \boldsymbol{e} \cdot \mathbf{C} \cdot \boldsymbol{e}_0 \qquad \text{with} \quad \mathbf{C} = \mathbf{F}^T \cdot \mathbf{F}, \tag{22}$$

where $\boldsymbol{e}$ and $\boldsymbol{e}_0$ denote the unit vectors of the fiber direction in the current and initial configuration, respectively.

2.2.4. *Weak form*

Let $\boldsymbol{w} \in W$ and $q \in Q$ be weighting functions for, respectively, the momentum equation and incompressibility constraint with W and Q defined as in Section 2.1.4; then after partial integration and substitution of the Neumann boundary conditions, the weak form of (15) is given by[1]

$$\int_{\Omega(t)} (\nabla \boldsymbol{w})^T : \boldsymbol{\sigma} \, d\Omega = \int_{\Omega(t)} \boldsymbol{w} \cdot \boldsymbol{f} \, d\Omega + \int_{\Gamma(t)} \boldsymbol{w} \cdot \boldsymbol{s} \, d\Gamma, \quad \forall \boldsymbol{w} \in W,$$

$$\int_{\Omega(t)} q(J - 1) \, d\Omega = 0, \qquad\qquad\qquad \forall q \in Q \tag{23}$$

Here $J = \det(\mathbf{F})$ is the Jacobian of the deformation. Note that the integrals are defined with respect to the current (unknown) configuration $\Omega(t)$ with boundary $\Gamma(t)$.

In order to evaluate the integrals, a transformation to a known (reference) configuration, denoted by Ω_r, is required. There are two options available: (i) a transformation back to the undeformed configuration (total Lagrange approach, $\Omega_r = \Omega_0$) or (ii) a transformation to the last known configuration (updated Lagrange approach, $\Omega_r = \Omega_n$); see Figure 1 for a schematic representation. In this work the updated Lagrange approach is used for describing the deformation of the continuum.

Let $\mathbf{F}_n$ denote the deformation tensor which describes the deformation from the initial configuration to the configuration Ω_n at $t = t_n$ and $\mathbf{F}_\Delta$ the deformation from configuration Ω_n to the current configuration; then the tensor describing the deformation from Ω_0 to the current configuration $\Omega(t)$ is given by

$$\mathbf{F} = \mathbf{F}_\Delta \cdot \mathbf{F}_n \tag{24}$$

with

$$\mathbf{F}_n = (\nabla_0 \boldsymbol{x}_n)^T \qquad \text{and} \qquad \mathbf{F}_\Delta = (\nabla_n \boldsymbol{x})^T, \tag{25}$$

---

[1]We will omit the additions $\forall \boldsymbol{w} \in W$ and $\forall q \in Q$ in the sequel of this paper.
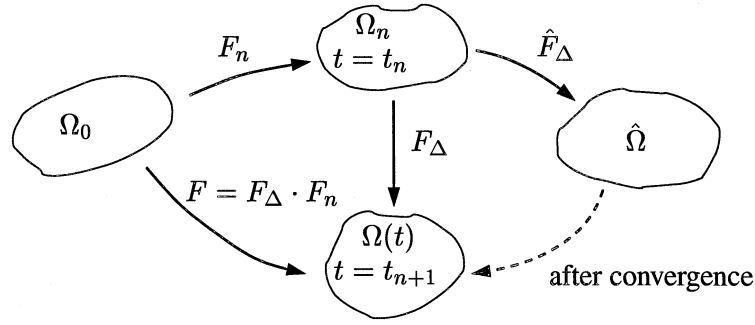
Figure 1. Schematic representation describing the deformation within an updated Lagrange approach.

where ∇_0 denotes the gradient operator with respect to the initial configuration and ∇_n denotes the gradient with respect to the known configuration Ω_n. Writing the gradient operator with respect to the current configuration[2] as $\nabla = \mathbf{F}_\Delta^{-T} \cdot \nabla_n$ yields the following weak form for the balance equations:

$$\int_{\Omega_n} (\nabla_n \boldsymbol{w})^T : \mathbf{F}_\Delta^{-1} \cdot \boldsymbol{\sigma} \, J_\Delta \, \mathrm{d}\Omega_n = \int_{\Omega_n} \boldsymbol{w} \cdot \boldsymbol{f} \, J_\Delta \, \mathrm{d}\Omega_n + \int_{\Gamma_n} \boldsymbol{w} \cdot \boldsymbol{s} \, \tilde{J}_\Delta \, \mathrm{d}\Gamma_n,$$

$$\int_{\Omega_n} q(J-1) \, J_\Delta \, \mathrm{d}\Omega_n = 0,$$

(26)

with $\mathrm{d}\Omega = J_\Delta \, \mathrm{d}\Omega_n$ and $\mathrm{d}\Gamma = \tilde{J}_\Delta \, \mathrm{d}\Gamma_n$.

2.2.5. *Linearization*

The nonlinear set of Equations (26) can be solved using a Newton iteration process. In the updated Lagrange formulation we take the last known configuration (Ω_n) to be the reference configuration (see 2.2.1 and Figure 1). If the converged solution (on Ω) is denoted by $\boldsymbol{x}$, and $\hat{\boldsymbol{x}}$ is an estimate of this solution (on $\hat{\Omega}$), then the variation $\delta\boldsymbol{x}$ in the estimate is given by $\delta\boldsymbol{x} = \boldsymbol{x} - \hat{\boldsymbol{x}}$.

All quantities appearing in (26) can be expanded similarly, giving

$$\mathbf{F}_\Delta = \mathbf{F}_\Delta + \delta\mathbf{F}_\Delta, \quad \boldsymbol{\sigma} = \hat{\boldsymbol{\sigma}} + \delta\boldsymbol{\sigma} = \hat{\boldsymbol{\sigma}} - \delta p\mathbf{I} + \delta\boldsymbol{\tau}, \quad J = \hat{J} + \delta J. \tag{27}$$

Note that, due to our choice, $\delta\mathbf{F}_\Delta$ does not represent the deformation for $\hat{\Omega}$ to Ω. After substitution of the expressions above in the balance equations and neglecting second-order

---

[2]This follows from $\nabla\boldsymbol{x} = \mathbf{I} = \mathbf{F}_\Delta^{-T} \cdot F_\Delta^T = \mathbf{F}_\Delta^{-T} \cdot \nabla_n\boldsymbol{x}$.

terms the linearized balance equations with respect to the reference configuration read

$$\int_{\Omega_n} (\nabla_n \boldsymbol{w})^T : \left(\delta(\mathbf{F}_\Delta^{-1}) \cdot \hat{\boldsymbol{\sigma}} + \mathbf{F}_\Delta^{-1} \cdot \left(-\delta p \mathbf{I} + \delta \boldsymbol{\tau} + \hat{\boldsymbol{\sigma}} \right) \right) \, J_\Delta \, \mathrm{d}\Omega_n =$$

$$\int_{\hat{\Omega}} \boldsymbol{w} \cdot \boldsymbol{f} \mathrm{d}\hat{\Omega} + \int_{\hat{\Gamma}} \boldsymbol{w} \cdot \boldsymbol{s} \mathrm{d}\hat{\Gamma}, \tag{28}$$

$$\int_{\Omega_n} q(\hat{J} + \delta J - 1) \, J_\Delta \, \mathrm{d}\Omega_n = 0.$$

Note that the right-hand side of (26) and (J_Δ) have been excluded from the linearization and are evaluated at the last known configuration in the iteration procedure. This does not break the theory but may influence the convergence rate. The body and surface forces are evaluated at the most recent configuration $\hat{\Omega}$ with boundary $\hat{\Gamma}$. Note that now all unknown quantities are with respect to the estimate $\hat{\boldsymbol{x}}$. If $\delta \boldsymbol{x}$ is sufficiently small, then $\delta(\mathbf{F}_\Delta^{-1})$ and δJ can be written as[3]:

$$\delta(\mathbf{F}_\Delta^{-1}) = -\mathbf{F}_\Delta^{-1} \cdot (\nabla \delta \boldsymbol{x})^T, \quad \delta J = \hat{J}(\nabla \cdot \delta \boldsymbol{x}) . \tag{29}$$

The linearized constitutive equations for the extra stress can be expressed in $\delta \boldsymbol{x}$ using $\delta \boldsymbol{\tau} = {}^4\mathbf{M} : (\nabla \delta \boldsymbol{x})^T$, where ${}^4\mathbf{M}$ is determined by the constitutive equation. It is convenient to rewrite the equations with respect to the most recent estimated configuration $\hat{\Omega}$ corresponding to position field $\hat{\boldsymbol{x}}$ by making use of (29). For the linearized balance equations with respect to the last known (estimated) configuration this gives

$$\int_{\hat{\Omega}} (\nabla \boldsymbol{w})^T : \left[\delta \boldsymbol{\tau} - (\nabla \delta \boldsymbol{x})^T \cdot \hat{\boldsymbol{\sigma}} \right] \mathrm{d}\hat{\Omega} - \int_{\hat{\Omega}} \delta p \nabla \cdot \boldsymbol{w} \, \mathrm{d}\hat{\Omega} =$$

$$\int_{\hat{\Omega}} \boldsymbol{w} \cdot \boldsymbol{f} \mathrm{d}\hat{\Omega} + \int_{\hat{\Gamma}} \boldsymbol{w} \cdot \boldsymbol{s} \mathrm{d}\hat{\Gamma} + \hat{r}, \tag{30}$$

$$\int_{\hat{\Omega}} q \nabla \cdot \delta \boldsymbol{x} \, \mathrm{d}\hat{\Omega} = -\int_{\hat{\Omega}} q \Big(\frac{\hat{J} - 1}{\hat{J}} \Big) \, \mathrm{d}\hat{\Omega}.$$

Here the residual $\hat{r}$ is defined by

$$\hat{r} = \int_{\hat{\Omega}} \left[-(\nabla \boldsymbol{w})^T : \hat{\boldsymbol{\tau}} + \hat{p}(\nabla \cdot \boldsymbol{w}) \right] \mathrm{d}\hat{\Omega}. \tag{31}$$

---

[3]We use:
$\mathbf{F}_\Delta^{-1} = (\mathbf{F}_\Delta + \delta \mathbf{F}_\Delta)^{-1} = [\mathbf{F}_\Delta \cdot (\mathbf{I} + \mathbf{F}_\Delta^{-1} \cdot \delta \mathbf{F}_\Delta)]^{-1} = (\mathbf{I} + \mathbf{F}_\Delta^{-1} \cdot \delta \mathbf{F}_\Delta)^{-1} \cdot \mathbf{F}_\Delta^{-1} \approx (\mathbf{I} - \mathbf{F}_\Delta^{-1} \cdot \delta \mathbf{F}_\Delta) \cdot \mathbf{F}_\Delta^{-1} = \mathbf{F}_\Delta^{-1} - \mathbf{F}_\Delta^{-1} \cdot \delta \mathbf{F}_\Delta \cdot \mathbf{F}_\Delta^{-1} = \mathbf{F}_\Delta^{-1} - \mathbf{F}_\Delta^{-1} \cdot (\mathbf{F}_\Delta^{-T} \cdot \delta \mathbf{F}_\Delta^T)^T = \mathbf{F}_\Delta^{-1} - \mathbf{F}_\Delta^{-1} \cdot (\mathbf{F}_\Delta^{-T} \cdot \nabla_n \delta \boldsymbol{x})^T = \mathbf{F}_\Delta^{-1} - \mathbf{F}_\Delta^{-1} \cdot (\nabla \delta \boldsymbol{x})^T$
and
$J = \det(\mathbf{F}) = \det(\mathbf{F} + \delta \mathbf{F}) = \det((\mathbf{I} + \delta \mathbf{F} \cdot \mathbf{F}^{-1}) \cdot \mathbf{F}) = \det(\mathbf{I} + \delta \mathbf{F} \cdot \mathbf{F}^{-1})\det(\mathbf{F}) \approx \hat{J}(1 + \mathrm{tr}(\delta \mathbf{F} \cdot \mathbf{F}^{-1})) = \hat{J} + \hat{J}\mathrm{tr}(\mathbf{F}^{-T} \cdot \delta \mathbf{F}^T)^T = \hat{J} + \hat{J}\mathrm{tr}(\mathbf{F}^{-T} \cdot \nabla_0 \delta \boldsymbol{x})^T = \hat{J} + \hat{J}\mathrm{tr}(\nabla \delta \boldsymbol{x})^T = \hat{J} + \hat{J}(\nabla \cdot \delta \boldsymbol{x}).$
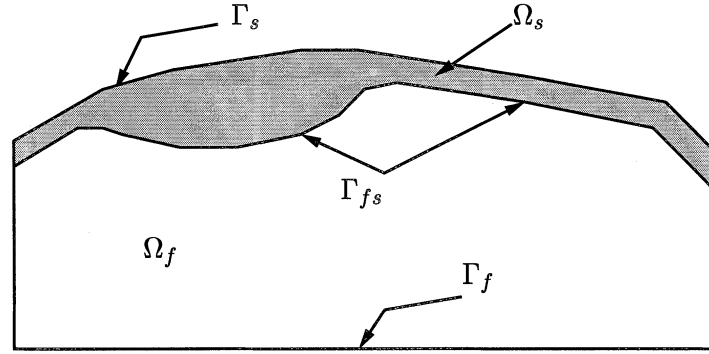
Figure 2. Schematic representation of a fluid domain Ω_f with boundary Γ_f partially connected to a solid domain Ω_s with boundary Γ_s.

Note that all quantities marked with a ˆ are known and that the gradient operator ∇ is taken with respect to the last known (estimated) configuration $\hat{\Omega}$. The natural boundary conditions are not included in the linearization process and are evaluated on $\hat{\Omega}$ and $\hat{\Gamma}$. The governing equations of (30) hold irrespective of the choice for the constitutive equation. To evaluate $\delta\boldsymbol{\tau}$ we need an expansion of the extra stress tensor $\boldsymbol{\tau}$ with respect to $\hat{\boldsymbol{\tau}}$ resulting from a variation in $\mathbf{F}$. For the neo-Hookean model (18) we find[4]:

$$\delta\boldsymbol{\tau} = G\left[(\nabla\delta\boldsymbol{x})^T \cdot \mathbf{B} + \mathbf{B} \cdot (\nabla\delta\boldsymbol{x})\right] \tag{32}$$

In general the variation $\delta\boldsymbol{\tau}$ is expressed in terms of the unknown parameter $\delta\boldsymbol{x}$ using $\delta\boldsymbol{\tau} = \mathbf{M} : (\nabla\delta\boldsymbol{x})^T$ where $\mathbf{M}$ is solely determined by the constitutive equation. For the fiber-reinforced material the linearization is identical for the isotropic matrix contribution. The variation in the stress can be derived as [22, p. 19]

$$\delta\boldsymbol{\tau} = \delta\boldsymbol{\tau}_m + \hat{\tau}_f(\mathbf{K} + \mathbf{K}^T) + 2\left(\hat{\lambda}_f^2 \left.\frac{\partial\tau_f}{\partial\lambda_f^2}\right|_{\lambda_f=\hat{\lambda}_f} - \hat{\tau}_f\right)K\hat{\boldsymbol{e}}\hat{\boldsymbol{e}}, \tag{33}$$

with

$$\mathbf{K} = (\nabla\delta\boldsymbol{x})^T \cdot \hat{\boldsymbol{e}}\hat{\boldsymbol{e}} \quad\text{and}\quad K = \hat{\boldsymbol{e}} \cdot (\nabla\delta\boldsymbol{x})^T \cdot \hat{\boldsymbol{e}}, \tag{34}$$

which are both linear tensor functions of $(\nabla\delta\boldsymbol{x})^T$.

2.3. ARBITRARY LAGRANGE-EULER METHODS (ALE)

2.3.1. *Coupling of reference systems*
We consider a fluid domain Ω_f bounded by Γ_f that is (partly) connected to a solid domain Ω_s with boundary Γ_s (see Figure 2). The interface boundary between Ω_f and Ω_s is denoted as $\Gamma_{fs} = \Gamma_f \cap \Gamma_s$. The deformation of the solid domain is either determined by the equations of motion given in the previous section, *i.e.*, (30) and (32), or prescribed. The deformation of the solid domain is formulated with respect to a changing configuration ($\hat{\Omega}$ in (30) of the previous section). The description of the fluid motion (9), however, is defined with respect to

---

$\overline{\delta\boldsymbol{\tau} \triangleq G\delta\mathbf{B}} = G[\delta\mathbf{F} \cdot \mathbf{F}^T + \mathbf{F} \cdot \delta\mathbf{F}^T] = G[(\nabla_0\delta\boldsymbol{x})^T \cdot \mathbf{F}^T + \mathbf{F} \cdot \nabla_0\delta\boldsymbol{x})] =$
$G[(\nabla_0\delta\boldsymbol{x})^T \cdot \mathbf{F}^{-1} \cdot \mathbf{F} \cdot \mathbf{F}^T + \mathbf{F} \cdot \mathbf{F}^T \cdot \mathbf{F}^{-T}(\nabla_0\delta\boldsymbol{x})] \approx G[(\nabla\delta\boldsymbol{x})^T \cdot \mathbf{B} + \mathbf{B} \cdot (\nabla\delta\boldsymbol{x})]$

a fixed domain Ω. The basis of an arbitrary Lagrange-Euler (ALE) formulation is the use of three separate coordinate systems: (i) the spatial or Eulerian reference system which is fixed in space, (ii) the material or Lagrangian reference system which moves with the material and (iii) the computational or arbitrary reference system which can move arbitrarily in space. A material point in the Lagrangian system is identified with its position vector x in the Eulerian system and with x_g in the computational reference system (computational grid). The physical quantities in the fluid-structure interaction problem are defined with respect to the Eulerian and Lagrangian system. Consequently, a finite-element formulation of a fluid-structure interaction problem can only be obtained if the Eulerian reference system is linked to the computational reference system.

Coupling of the grid with the Eulerian system is achieved by considering the evolution of a state variable $\phi(x, t)$ in material point P defined in the Lagrangian system. During an infinitesimally small time step Δt, the position of P with respect to the Eulerian system changes according to

$$x(t) \rightarrow x(t + \Delta t) = x + \mathrm{d}x \quad \text{for } t \rightarrow t + \Delta t. \tag{35}$$

The material derivative for $\Delta t \rightarrow 0$ can be written as

$$\frac{\mathrm{D}\phi}{\mathrm{D}t} = v \cdot (\nabla \phi) + \left.\frac{\partial \phi}{\partial t}\right|_x, \tag{36}$$

where v is the velocity of the material point and ∇ the gradient operator with respect to the Eulerian system. With respect to the grid reference system, the position of material point P changes according to

$$x_g(t) \rightarrow x_g(t + \Delta t) = x_g(t) + (\mathrm{d}x - \mathrm{d}x_g) \quad \text{for } t \rightarrow t + \Delta t, \tag{37}$$

with $\mathrm{d}x_g$ the change in position of x_g. Using the previous equation with (36), we have for the material derivative

$$\frac{\mathrm{D}\phi}{\mathrm{D}t} = (v - v_g) \cdot (\nabla \phi) + \left.\frac{\partial \phi}{\partial t}\right|_{x_g}, \tag{38}$$

with v_g the grid velocity and where ∇ remains with respect to the Eulerian system. Note that $\partial \phi / \partial t$ is now defined with respect to the grid point x_g. Application to the momentum equation yields

$$\rho \left(\left.\frac{\partial v}{\partial t}\right|_{x_g} + (v - v_g) \cdot \nabla v \right) = \nabla \cdot \sigma + f \qquad \text{in } \Omega_f. \tag{39}$$

Compared with (1) the grid velocity appears in the convective term and the time derivative is now defined with respect to the grid points x_g.

2.3.2. *Weak formulation*
If the grid velocity at $t = t^n$ is denoted by v_g^n and is assumed to be constant during the time interval from t^n to t^{n+1}, the linearization of the convective term yields

$$\left(\hat{v} + \delta v - v_g^n \right) \cdot \nabla \left(\hat{v} + \delta v \right) \approx (\hat{v} - v_g^n) \cdot \nabla \hat{v} + (\hat{v} - v_g^n) \cdot \nabla \delta v + \delta v \cdot \nabla \hat{v}, \tag{40}$$

when higher-order terms are neglected. In the weak formulation given in (9), due to the moving grid, the convective term will change according to

$$\left[\hat{v} \cdot \nabla \delta v \right]_{(9)} \rightarrow (\hat{v} - v_g^n) \cdot \nabla \delta v. \tag{41}$$
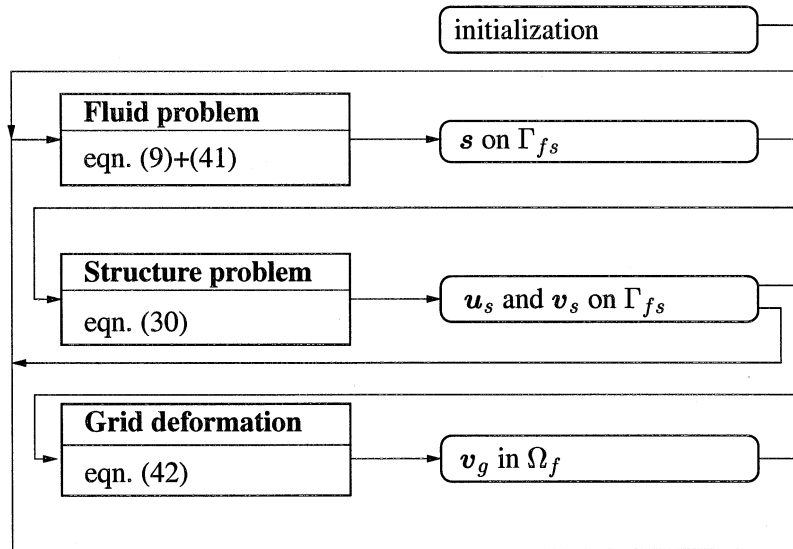
Figure 3. Schematic representation of a ALE method.

The approximation of the local time derivative with respect to the grid points is defined exactly by (10) as $\boldsymbol{v}$ and $\boldsymbol{v}^n$ are evaluated in the same grid point and thereby in different locations in the Eulerian reference system.

The motion of the grid defined by grid velocity $\boldsymbol{x}_g$ depends on the deformation of the solid mesh. A proper fluid-mesh quality is preserved by computing a fluid-grid displacement field $\boldsymbol{u}_g$ from a standard linear elastic deformation problem defined in Ω_f:

$$\int_{\Omega_f} \boldsymbol{\epsilon}_{w_g} : ({}^4\mathbf{C} : \boldsymbol{\epsilon}_{u_g})\, \mathrm{d}\Omega_g = 0 \qquad \text{in } \Omega_f, \tag{42}$$

with the displacement at the boundary equal to the displacement of the solid at Γ_{fs} and zero elsewhere:

$$\boldsymbol{u}_g = \begin{cases} \delta\boldsymbol{x} & \text{at } \Gamma_{fs} \\ \boldsymbol{0} & \text{at } \Gamma_f / \Gamma_{fs} \end{cases}. \tag{43}$$

In these equations ${}^4\mathbf{C}$ is the fourth-order Hookean elasticity tensor for a linear elastic compressible solid, $\boldsymbol{\epsilon}_{u_g} = \frac{1}{2}[\nabla\boldsymbol{u}_g + (\nabla\boldsymbol{u}_g)^T]$ the elastic strain tensor and $\boldsymbol{\epsilon}_{w_g}$ its variational counterpart with respect to the weighting function $\boldsymbol{w}_g \in \boldsymbol{W}$.

The solution procedure for the ALE method is shown in Figure 3. In the fluid problem the velocity field in Ω_f is computed using inflow velocity and the velocity of the moving solid boundary as boundary conditions. From this velocity field the traction vector $\boldsymbol{s}$ on Γ_{fs} can be computed and used as boundary condition for the structure problem. In the structure problem the deformation of the solid domain Ω_s is computed providing boundary conditions $\boldsymbol{u}_s$ and $\boldsymbol{v}_s$ for the grid-deformation problem and the fluid problem, respectively. Finally, the grid-deformation problem is solved to obtain $\boldsymbol{v}_g$ needed for the fluid problem.
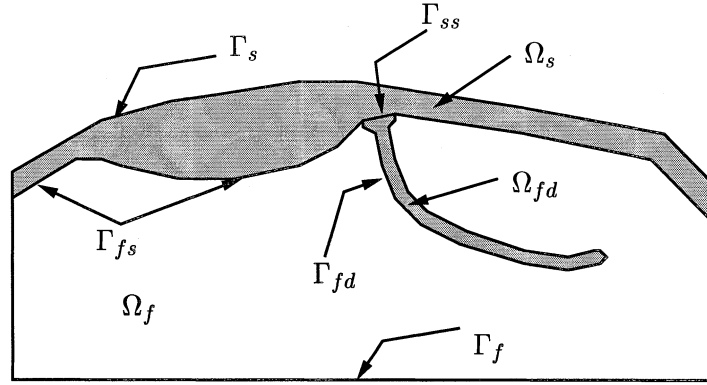
Figure 4. Schematic representation of a solid domain $\Omega_{fd} \subset \Omega_s$ with boundary Γ_{fd} immersed in a fluid domain Ω_f with boundary Γ_f.

2.4. FICTITIOUS-DOMAIN METHODS (FD)

2.4.1. *Fluid-structure interface conditions*

We consider a solid domain $\Omega_{fd} \subset \Omega_s$ that is immersed in a fluid domain Ω_f and separated from the solid domain Ω_s by the boundary Γ_{ss}. The interface between the fluid domain Ω_f and the immersed solid domain Ω_{fd} is denoted by Γ_{fd} (fictitious-domain boundary). Continuity of stress at the interface between the solid on the fluid is given by

$$\boldsymbol{\sigma}_{sf} \cdot \boldsymbol{n}_f + \boldsymbol{\sigma}_{fs} \cdot \boldsymbol{n}_s = \boldsymbol{0} \qquad \text{at } \Gamma_{fd}, \tag{44}$$

with $\boldsymbol{n}_f$ the outward-directed normal of the fluid domain and $\boldsymbol{n}_s$ the outward-directed normal of the solid domain, *i.e.*, the opposite direction, at Γ_{fd}. In terms of surface tractions exerted by the solid on the fluid $\boldsymbol{s}_{sf}$ and the fluid on the solid $\boldsymbol{s}_{fs}$, this can also be written as

$$\boldsymbol{s}_{sf} = -\boldsymbol{s}_{fs} \qquad \text{at } \Gamma_{fd}. \tag{45}$$

In the fictitious-domain method, however, the fluid does not have a explicitly defined boundary at the interface with the immersed solid. In the original formulations of the fictitious-domain method [13, 17, 18, 23] a variational approach is used and the coupling between fluid and structure is established by means of Lagrange multipliers. In this work, the weak form of the equations of motion is used to formulate the same fictitious-domain approach. In this formulation, the traction exerted by the solid on the fluid is regarded as a *locally* acting unknown body force $\boldsymbol{f}$ in the fluid domain. With the use of the Dirac delta function, this force can be written as:

$$\boldsymbol{f} = \bar{\boldsymbol{s}}_{sf} \delta(\boldsymbol{x} - \boldsymbol{x}_{\Gamma_{fd}}) \qquad \text{on } \Omega_f. \tag{46}$$

In this way the *global* body force $\boldsymbol{f}$ is localized at the interface by means of the delta function. Here $\bar{\boldsymbol{s}}_{sf}$ defined on Ω_f is chosen such that $\bar{\boldsymbol{s}}_{sf} = \boldsymbol{s}_{sf}$ on Γ_{fd} and (45) is satisfied.

The kinematic coupling at the interface Γ_{fd} is enforced using the boundary condition

$$\boldsymbol{v}_f = \boldsymbol{v}_s = \dot{\boldsymbol{x}}_s \qquad \text{at } \Gamma_{fd}, \tag{47}$$

with $\boldsymbol{v}_f$ and $\boldsymbol{v}_s$, respectively, the fluid and solid velocity and $\dot{\boldsymbol{x}}_s$ the time derivative of the (solid) displacement field.

2.4.2. *Weak formulation*

With the application of the fictitious-domain method, the weak formulations of the fluid and the solid equations of motion are altered. The interaction between the fluid and solid domain is included in the balance equations using the body force in the fluid domain and the surface traction in the solid domain. Making use of the properties of the delta function, we can write for the body force in (9):

$$\int_{\Omega} \boldsymbol{w} \cdot \boldsymbol{f}\, \mathrm{d}\Omega = \int_{\Omega_f} \boldsymbol{w}_f \cdot \boldsymbol{s}_{sf} \delta(\boldsymbol{x} - \boldsymbol{x}_{\Gamma fd})\, \mathrm{d}\Omega_f = -\int_{\Gamma_{fd}} \boldsymbol{w}_f \cdot \boldsymbol{s}_{fd}\, \mathrm{d}\Gamma_{fd}, \tag{48}$$

with $\boldsymbol{s}_{fd}$ the unknown traction at the fictitious-domain boundary and $\boldsymbol{w}_f$ the weighting function for the fluid domain. The interface condition (45) is then satisfied weakly if the surface traction in (30) is written as:

$$\int_{\hat{\Gamma}} \boldsymbol{w} \cdot \boldsymbol{s}\, \mathrm{d}\hat{\Gamma} = \int_{\hat{\Gamma}_{fd}} \boldsymbol{w}_s \cdot \boldsymbol{s}_{fd}\, \mathrm{d}\hat{\Gamma}_{fd}, \tag{49}$$

with $\boldsymbol{w}_s$ the weighting functions for the solid domain.

The interaction surface traction $\boldsymbol{s}_{fd}$ can be interpreted as a Lagrange multiplier to weakly couple the velocities of the fluid and the solid through

$$\int_{\Gamma_{fd}} \boldsymbol{w}_{fd} \cdot (\boldsymbol{v}_f - \boldsymbol{v}_s)\, \mathrm{d}\Gamma_{fd} = 0, \qquad \text{in } \Gamma_{fd}, \tag{50}$$

with $\boldsymbol{w}_{fd}$ the weighting functions defined on the fluid-solid-interaction interface.

2.5. ARBITRARY LAGRANGE-EULER FICTITIOUS-DOMAIN METHODS (ALE-FD)

For a fluid-structure interaction problem with ALE formulation and fictitious-domain incorporated, the linearized weak formulation for the fluid, solid and their coupling obtained with the weighted-residuals method is summarized in (51) to (53). The equations for fluid motion resulting from, respectively, the momentum and mass-balance equations are given by:

$$\int_{\Omega_f} \boldsymbol{w}_f \cdot \rho \left(\left. \frac{\delta \boldsymbol{v}}{\Delta t} \right|_{\boldsymbol{x}_g} + (\hat{\boldsymbol{v}} - \boldsymbol{v}_g^n) \cdot \nabla \delta \boldsymbol{v} + \delta \boldsymbol{v} \cdot \nabla \hat{\boldsymbol{v}} \right)\, \mathrm{d}\Omega_f +$$

$$+ \int_{\Omega_f} (\nabla \boldsymbol{w}_f)^T : \delta \boldsymbol{\tau}_f\, \mathrm{d}\Omega_f - \int_{\Omega_f} (\nabla \cdot \boldsymbol{w}_f) \delta p_f\, \mathrm{d}\Omega + \int_{\Gamma_{fd}} \boldsymbol{w}_f \cdot \delta \boldsymbol{s}_{fd}\, \mathrm{d}\Gamma_{fd}$$

$$= -\int_{\Gamma_{fd}} \boldsymbol{w}_f \cdot \hat{\boldsymbol{s}}_{fd}\, \mathrm{d}\Gamma_{fd} + \int_{\Gamma_f} \boldsymbol{w}_f \cdot \boldsymbol{s}_f\, \mathrm{d}\Gamma_F + \hat{r}_f, \tag{51}$$

$$\int_{\Omega_f} q_f (\nabla \cdot \delta \boldsymbol{v})\, \mathrm{d}\Omega_f = -\int_{\Omega_f} q_f (\nabla \cdot \hat{\boldsymbol{v}})\, \mathrm{d}\Omega_f.$$

The deformation of the structure is captured in the balance of momentum and the incompressibility constraint:

$$\int_{\Omega_s} (\nabla \boldsymbol{w}_s)^T : \left(\delta \boldsymbol{\tau}_s - (\nabla \delta \boldsymbol{x})^T \cdot \hat{\boldsymbol{\sigma}}_s \right) \, \mathrm{d}\Omega_s - \int_{\Omega_s} \delta p_s \nabla \cdot \boldsymbol{w}_s \, \mathrm{d}\Omega_s - \int_{\Gamma_{fd}} \boldsymbol{w}_s \cdot \delta \boldsymbol{s}_{fd} \, \mathrm{d}\Gamma_{fd}$$
$$= \int_{\Gamma_s} \boldsymbol{w}_s \cdot \boldsymbol{s}_s \, \mathrm{d}\Gamma_s + \int_{\Gamma_{fd}} \boldsymbol{w}_s \cdot \hat{\boldsymbol{s}}_{fd} \, \mathrm{d}\Gamma_{fd} + \hat{r}_s, \tag{52}$$

$$\int_{\Omega_s} q_s \nabla \cdot \delta \boldsymbol{x} \, \mathrm{d}\Omega_s = - \int_{\Omega_s} q_s \left(\frac{\hat{J} - 1}{\hat{J}} \right) \mathrm{d}\Omega_s.$$

Finally, the coupling between fluid and solid as defined by the fictitious-domain method is given by:

$$\int_{\Gamma_{fd}} \boldsymbol{w}_{fd} \cdot (\delta \boldsymbol{v}_f - \delta \boldsymbol{v}_s) \, \mathrm{d}\Gamma_{fd} = - \int_{\Gamma_{fd}} \boldsymbol{w}_{fd} \cdot (\hat{\boldsymbol{v}}_f - \hat{\boldsymbol{v}}_s) \, \mathrm{d}\Gamma_{fd} \tag{53}$$

Here we used the following two definitions for the fluid and solid residual respectively:

$$\hat{r}_f = \int_{\Omega_f} \boldsymbol{w}_f \cdot \rho \left(\frac{\boldsymbol{v}_f^n - \hat{\boldsymbol{v}}_f}{\Delta t} - (\hat{\boldsymbol{v}}_f - \boldsymbol{v}_g) \cdot \nabla \hat{\boldsymbol{v}}_f \right) \, \mathrm{d}\Omega_f +$$
$$+ \int_{\Omega_f} \left[-(\nabla \boldsymbol{w}_f)^T : \hat{\boldsymbol{\tau}}_f + \hat{p}_f \nabla \cdot \boldsymbol{w}_f \right] \, \mathrm{d}\Omega_f \tag{54}$$

and

$$\hat{r}_s = \int_{\Omega_s} \left[-(\nabla \boldsymbol{w}_s)^T : \hat{\boldsymbol{\tau}}_s + \hat{p}_s (\nabla \cdot \boldsymbol{w}_s) \right] \, \mathrm{d}\Omega_s. \tag{55}$$

In Figure 5 the ALE-FD method is shown schematically. For each iteration the fluid problem and the structure problem are solved simultaneously together with the coupling constraint. The solution of this coupled problem is checked for convergence with respect to the fluid velocity $\boldsymbol{v}_f$, solid displacement $\boldsymbol{u}_s$ and surface traction $\boldsymbol{s}_{fs}$. At convergence the solid deformation $\boldsymbol{u}_s$ at boundary Γ_{fs} is used as a boundary condition for grid deformation. The resulting grid velocity $\boldsymbol{v}_g$ is then transferred to the next time step.

3. Finite-element formulation

3.1. FINITE-ELEMENT APPROXIMATION

In order to obtain a discrete set of finite-element equations, the complete domains Ω_f and Ω_s, as well as the fictitious-domain boundary Γ_{fd}, are divided into non-overlapping sub-domains Ω_f^e, Ω_s^e and Γ_{fd}^e, respectively. Within each element the unknowns $\delta \boldsymbol{v}_\alpha$, δp_α and $\delta \boldsymbol{s}_{fd}$ are
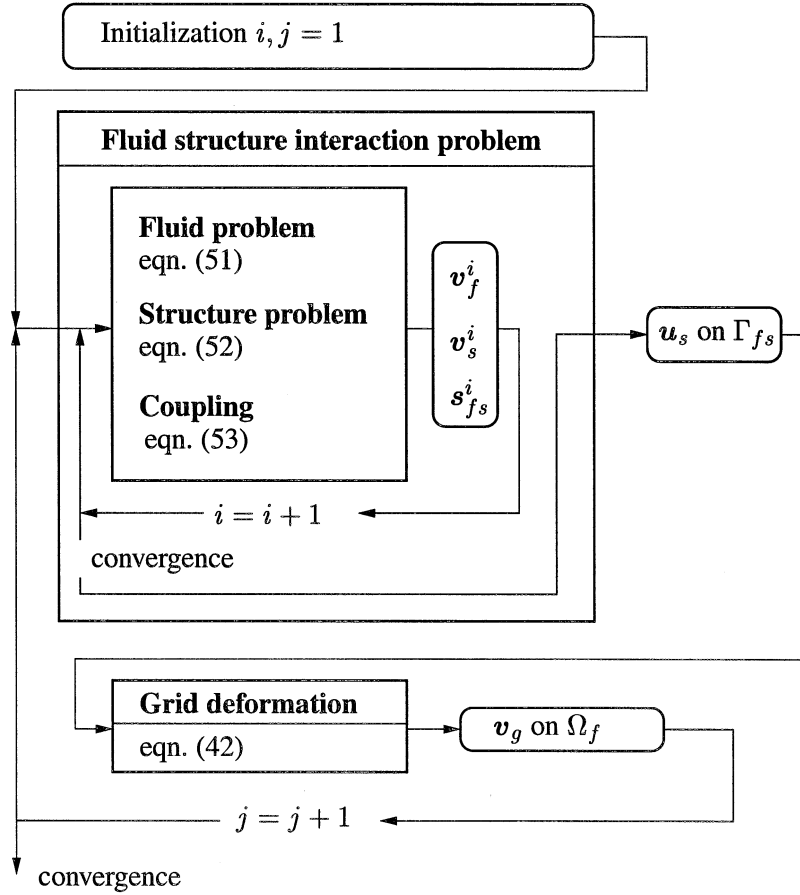
Figure 5. Schematic representation of a ALE-FD method.

approximated by δv_α^e, δp_α^e and δs_{fd}^e using Lagrange interpolation polynomials defined by the predefined nodes per element, *i.e.*:

$$\delta v_\alpha^e(x, t) = \sum_{i=1}^{n_v} \varphi_i(x) \delta v_{\alpha,i}^e(t) = \underset{\sim}{\varphi}^T \delta \underset{\sim}{v}_\alpha^e \qquad \forall x \in \Omega_\alpha^e , \alpha = f, s \tag{56}$$

with n_v being the number of velocity interpolation points per volume element Ω_α^e; $\underset{\sim}{\varphi} = [\varphi_1, \ldots, \varphi_{n_v}]^T$ is the column of velocity shape functions φ_i, and $\delta \underset{\sim}{v}_\alpha^e = [\delta v_{\alpha,1}^e, \ldots, \delta v_{\alpha,n}^e]^T$ the column that contains the unknowns $\delta v_{\alpha,i}^e$ per element.

$$p_\alpha^e(x, t) = \sum_{i=1}^{n_p} \psi_i(x) p_{\alpha,i}^e(t) = \underset{\sim}{\psi}^T \underset{\sim}{p}_\alpha^e \qquad \forall x \in \Omega_\alpha^e , \alpha = f, s. \tag{57}$$

Here n_p is the number of pressure interpolation points per volume element Ω_α^e, $\underset{\sim}{\psi} = [\psi_1, \ldots, \psi_{n_v}]^T$ is the column of pressure shape functions ψ_i, and $\delta \underset{\sim}{p}_\alpha^e = [\delta p_{\alpha,1}^e, \ldots, \delta p_{\alpha,n}^e]^T$ the column that contains the pressure unknowns $\delta p_{\alpha,i}^e$ per element.

$$\delta s_{fd}^e(x, t) = \sum_{i=1}^{n_{fd}} \phi_i(x) \delta s_{fd,i}^e(t) = \underset{\sim}{\phi}^T \delta \underset{\sim}{s}_{fd}^e \qquad \forall x \in \Gamma_{fd}^e, \tag{58}$$

where n_{fd} is the number of surface-traction interpolation points per interface element Γ^e_{fd}, $\underset{\sim}{\phi} = [\phi_1, \ldots, \phi_{n_{fd}}]^T$ is the column of surface-traction shape functions ϕ_i, and $\delta \underset{\sim}{s}^e_{fd} = [\delta s^e_{fd,1}, \ldots, \delta s^e_{fd,n}]^T$ the column that contains the surface-traction unknowns $\delta s^e_{fd,i}$ per interface element.

The weighting functions $\boldsymbol{w}^e_\alpha$, q^e_α and $\boldsymbol{w}^e_{fd}$ are discretized with the corresponding shape functions (Galerkin method), *i.e.*:

$$\boldsymbol{w}^e_\alpha(\boldsymbol{x}) = \sum_{i=1}^{n_v} \varphi_i(\boldsymbol{x}) \boldsymbol{w}^e_{\alpha,i} = \underset{\sim}{\varphi}^T \underset{\sim}{\boldsymbol{w}}^e_\alpha \qquad \forall \boldsymbol{x} \in \Omega^e_\alpha \,, \alpha = f, s, \tag{59}$$

$$q^e_\alpha(\boldsymbol{x}) = \sum_{i=1}^{n_p} \psi_i(\boldsymbol{x}) q^e_{\alpha,i} = \underset{\sim}{\psi}^T \underset{\sim}{q}^e_\alpha \qquad \forall \boldsymbol{x} \in \Omega^e_\alpha \,, \alpha = f, s, \tag{60}$$

$$\boldsymbol{w}^e_{fd}(\boldsymbol{x}, t) = \sum_{i=1}^{n_{fd}} \phi_i(\boldsymbol{x}) \boldsymbol{w}^e_{fd,i} = \underset{\sim}{\phi}^T \underset{\sim}{\boldsymbol{w}}^e_{fd} \qquad \forall \boldsymbol{x} \in \Gamma^e_{fd}. \tag{61}$$

In the next section the choice of the shape functions $\varphi_i(\boldsymbol{x})$, $\psi_i(\boldsymbol{x})$ and $\phi_i(\boldsymbol{x})$ will be discussed. Substitution of the approximations (56), (57) and (58) and the weighting functions (59), (60) and (61) in the weak forms (51), (52) and (53) and summation over the finite-element domains yields a finite-element discrete set of equations with a structure given by:

$$\left(\begin{bmatrix} \underline{S}_f & \underline{L}_f^T \\ \underline{L}_f & \underline{0} \end{bmatrix} \quad \begin{bmatrix} & & \\ & \underline{0} & \end{bmatrix} \quad \begin{bmatrix} \underline{L}_{fc}^T \\ \underline{0} \end{bmatrix} \\ \begin{bmatrix} & & \\ & \underline{0} & \end{bmatrix} \quad \begin{bmatrix} \underline{S}_s & \underline{L}_s^T \\ \underline{L}_s & \underline{0} \end{bmatrix} \quad \begin{bmatrix} \underline{L}_{sc}^T \\ \underline{0} \end{bmatrix} \\ \begin{bmatrix} \underline{L}_{fc} & \underline{0} \end{bmatrix} \quad \begin{bmatrix} \underline{L}_{sc} & \underline{0} \end{bmatrix} \quad \begin{bmatrix} \underline{0} \end{bmatrix} \right) \cdot \begin{pmatrix} \delta \underset{\sim}{v}_f \\ \delta \underset{\sim}{p}_f \\ \delta \underset{\sim}{v}_s \\ \delta \underset{\sim}{p}_s \\ \delta \underset{\sim}{s}_{fd} \end{pmatrix} = \begin{pmatrix} \underset{\sim}{f}^v_f \\ \underset{\sim}{f}^p_f \\ \underset{\sim}{f}^v_s \\ \underset{\sim}{f}^p_s \\ \underset{\sim}{f}^s_{fd} \end{pmatrix} \tag{62}$$

with $\delta \underset{\sim}{v}_\alpha = [\delta \underset{\sim}{v}_{\alpha,1} \, \delta \underset{\sim}{v}_{\alpha,2} \, \delta \underset{\sim}{v}_{\alpha,3}]^T$, $\underline{S}_f$ and $\underline{S}_s$ the fluid and solid system matrices, $\underline{L}_f$ and $\underline{L}_s$ the divergence matrices for the fluid and solid and finally $\underline{L}_{fc}$ and $\underline{L}_{sc}$ the fluid-structure coupling matrices.

3.2. Finite-element spaces

In the previous section the structure of the element stiffness matrix and the element vector have been derived based on the weak form of the equations of motion. To compute these matrices, the specific shape functions and their derivatives for the displacement, the pressure and the traction vector are needed. Also, numerical integration procedures to compute the coefficients of the element vector and element matrix have to be defined. These quantities are all dependent on the element shape and the order of interpolation.

A widely used classifying method for elements used in the mixed finite-element method is to consider the type of pressure approximation being used. Two classes are distinguished, *i.e.*, continuous pressure approximations and discontinuous pressure approximations. The former
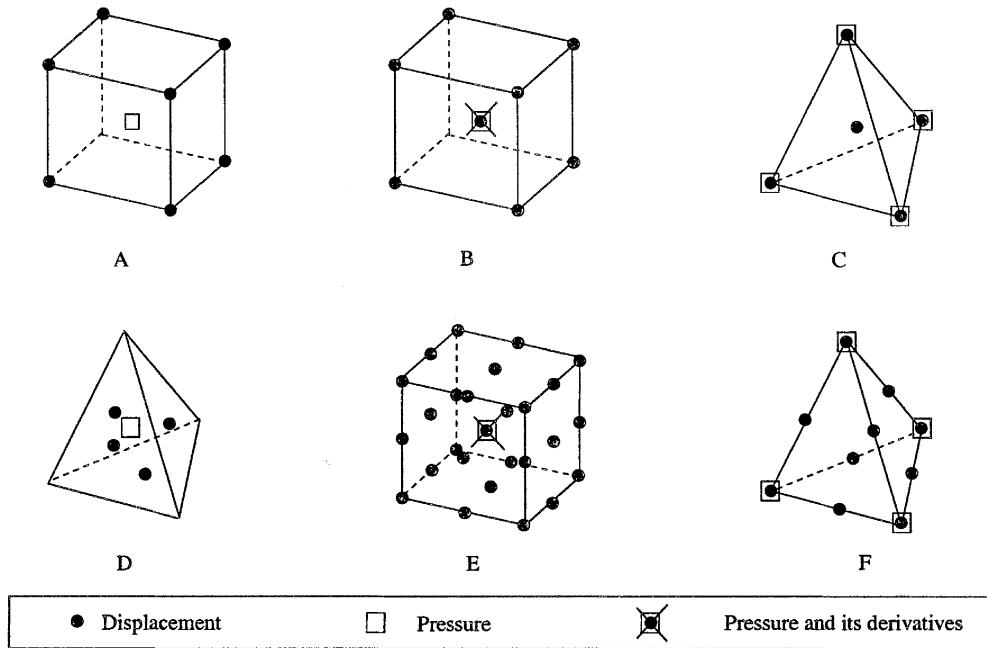
Figure 6. Three-dimensional elements: *A*) $Q_1 - P_0$ hexahedron, *B*) $Q_1^+ - P_1$ discontinuous pressure hexahedron, *C*) $Q_1^+ - P_1$ continuous tetrahedron (MINI element), *D*) nonconforming $Q_1 - P_0$ element, *E*) $Q_2^+ - P_1$ discontinuous pressure hexahedron, *F*) $Q_2 - P_1$ Taylor-Hood tetrahedron (continuous pressure).

are also known as Taylor-Hood elements and the latter as Crouzeix-Raviart elements. Here mainly Crouzeix-Raviart elements are treated because they allow discontinuity of the pressure at each interface of the elements as can be desired in many cases in cardiovascular mechanics in which fluid-structure interaction is involved [19].

A widely used element for three-dimensional analysis is the $Q_1 - P_0$-element. This discontinuous hexahedral element uses trilinear interpolation functions for the displacement at the vertices and a constant pressure in its centroid. A major drawback is that this element is not a compatible element. The theoretical compatibility condition for mixed finite-element methods, the Babuška-Brezzi condition, must be satisfied in order to ensure reliable computations. The $Q_1 - P_0$ element is therefore unsafe owing to the possibility of locking. Compatible elements of the discontinuous class, developed by Fortin [5] and tested by Robichaud and Tanguy [6], are the $Q_1^+ - P_0$, the $Q_1^+ - P_1$ and the $Q_1^{++} - P_1$ elements. It was shown that these enriched elements maintain the advantage of low computational costs of the $Q_1 - P_0$ element. The $Q_1^+ - P_1$ is considered the best choice when an accurate pressure determination is needed. A tetrahedral counterpart of this element would be the so-called MINI element (See Figure 6 C). Together with the non-conforming $Q_1 - P_0$-element this is probably the most simple stable three-dimensional element.

Apart from linear approximations for the displacement, quadratic approximations can also be used. Not only is the accuracy improved, but also a better description of the geometry can be realized. For instance, curved edges can be approximated much better using quadratic elements. A well-known element of this type is the $Q_2 - P_1$ hexahedral element, which does satisfy the compatibility condition, but is very expensive for practical computations because of the 85 degrees of freedom. This element can also be used as a continuous (Taylor-Hood)
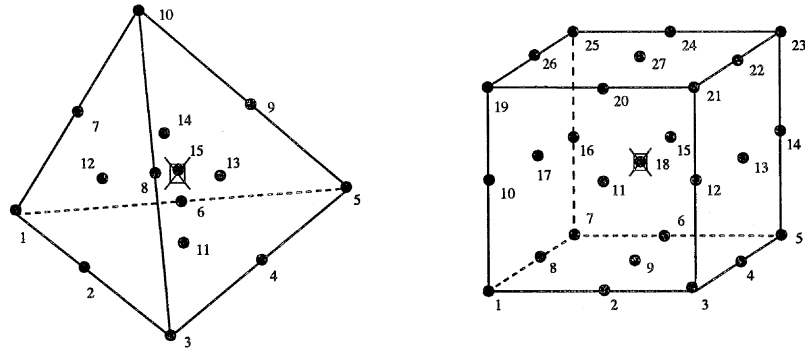
Figure 7. Three-dimensional Crouzeix-Raviart elements. The $P_2^+ P_1$ tetrahedral element (left) and the $Q_2^+ P_1$ hexahedral element (right).

pressure element. A continuous tetrahedral counterpart that is frequently used is the $Q_2 - P_1$-element. This element has four nodes in the vertices and six at the midpoints of each element edge. The pressure will be approximated linearly in the vertices, while the displacements are interpolated in all ten nodes.

From the above a tetrahedral analogue seems to be more efficient in terms of computational costs. However a discontinuous pressure approximation is desired. Therefore a Crouzeix-Raviart tetrahedron can provide a solution. In two-dimensional space a commonly used discontinuous triangular element exists which can be extended to three dimensions. This 3-D analogue yields the $Q_2^+ - P_1$ tetrahedron, which satisfies the Babuška-Brezzi condition [24]. So far this element has not been used very often. This element has a much larger number of degrees of freedom compared to the $Q_2 - P_1$ tetrahedron, *i.e.*, 45 in displacement and 4 in pressure. The additional degrees of freedom are a consequence of the 5 newly created nodes. The four nodes in the centers of the faces as proposed by Brezzi and Fortin [24] enable to control the normal flow on these faces and finally a node in the centroid of the tetrahedron is added to stabilize the non-constant part of the pressure.

In this paper two element shapes will be considered, the $P_2^+ P_1$ tetrahedral element and the $Q_2^+ P_1$ hexahedral element, both of the Crouzeix-Raviart type with an extended quadratic approximation for the velocity and a discontinuous linear approximation for the pressure.

In Figure 7 the three-dimensional Crouzeix-Raviart elements are presented. Note that the centroidal nodes have seven degrees of freedom, *i.e.*, three displacements corresponding to the Cartesian coordinates and four for the pressure and its derivatives. So the following finite-element spaces will be used:

tetrahedral:

$$\boldsymbol{W}^h = \{\boldsymbol{w} \in [H_0^1(\Omega)]^3; \boldsymbol{w}^e = \boldsymbol{w}^h|_{\Omega^e} \in [P_2^+(\Omega^e)]^3\},$$

$$Q^h = \{q \in L_0^2(\Omega); q^e = q^h|_{\Omega^e} \in P_1(\Omega^e)\};$$

(63)

hexahedral:

$$\boldsymbol{W}^h = \{\boldsymbol{w} \in [H_0^1(\Omega)]^3; \boldsymbol{w}^e = \boldsymbol{w}^h|_{\Omega^e} \in [Q_2^+(\Omega^e)]^3\},$$

$$Q^h = \{q \in L_0^2(\Omega); q^e = q^h|_{\Omega^e} \in P_1(\Omega^e)\}.$$

(64)

Although in many cases a linear approximation can also be used, for the surface traction unknown at the fictitious-domain interface a piecewise constant approximation turned out to be a good choice, as a quadratic approximation in many cases results in an over-constrained coupling, *i.e.*:

coupling:

$$\boldsymbol{W}^h_{fd} = \{\boldsymbol{w}_{fd} \in [L^2_0(\Gamma)]^3; \boldsymbol{w}^e_{fd} = \boldsymbol{w}^h_{fd}|_{\Gamma^e} \in [P_0(\Gamma^e)]^3\}. \tag{65}$$

In the next section a comparison of the performance of the two elements for fluid flow and solid deformation will be made. Application to fluid-structure interaction problems will be presented in the subsequent section.

3.3. SOLUTION METHOD

The linearized system of algebraic equations associated with the fluid, structure, grid deformation and fluid-structure interaction problems can not practically be solved with a direct solver because of the large number of degrees of freedom involved. Due to the structure and ill-conditioning of the matrix system, convergence of a straightforward applied iterative solver would be very slow. In the software used in this study [25] a special renumbering of degrees of freedom and an incomplete ILU preconditioned BiCGStab iterative solver is used [25].

4. Numerical tests

4.1. FLUID FLOW

In this chapter the $P^+_2 P_1$ tetrahedral element depicted in Figure 7 will be evaluated for fluid flow and compared to the hexahedral $Q^+_2 P_1$ element given in the same figure. This 27-noded brick is used as a reference for costs and convergence criteria. A boundary-value problem of which the exact solution is known will be implemented and the simulation results will be compared to their analytical solution. These simulations will be executed using several mesh sizes and their results will be evaluated.

4.1.1. *Beltrami test*
When evaluating a Navier-Stokes solver, numerical results can be compared with the exact solution, if available. Most of these exact solutions, however, are degenerate in the sense that certain terms in the governing equations are equal to zero and as a consequence interactions between the different terms are not tested. In order to test a Navier-Stokes solver without the unsteady, convective, pressure or diffusion terms being zero, a special 3D solution of the Navier-Stokes equations was developed by Ethier and Steinman [26]. In this so-called Beltrami flow, as presented in Equations (66) and (67), the unsteady terms balance the diffusion terms, while the convective terms balance the pressure gradient.

$$
\begin{aligned}
v_x &= -a[\mathrm{e}^{ax}\sin(ay \pm dz) + \mathrm{e}^{az}\cos(ax \pm dy)]\mathrm{e}^{-d^2t}, \\
v_y &= -a[\mathrm{e}^{ay}\sin(az \pm dx) + \mathrm{e}^{ax}\cos(ay \pm dz)]\mathrm{e}^{-d^2t}, \\
v_z &= -a[\mathrm{e}^{az}\sin(ax \pm dy) + \mathrm{e}^{ay}\cos(az \pm dx)]\mathrm{e}^{-d^2t},
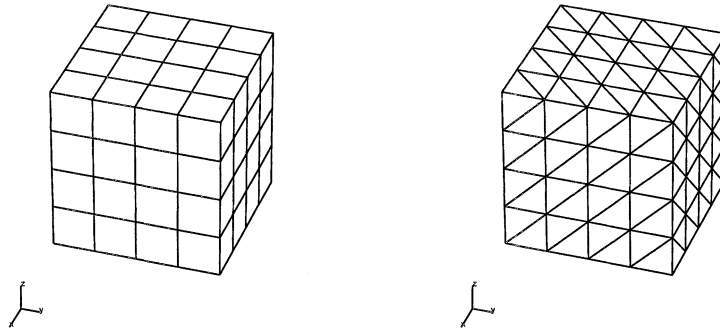\end{aligned}
\tag{66}
$$

Figure 8. Cubes used for the Beltrami test with a hexahedral mesh (left) and a tetrahedral mesh (right), both with a nodal spacing of 0·25.

$$
\begin{aligned}
p = -\frac{a^2}{2}[&e^{2ax} + 2\sin(ax \pm dy)\cos(az \pm dx)e^{a(y+z)} + \\
+ &e^{2ay} + 2\sin(ay \pm dz)\cos(ax \pm dy)e^{a(z+x)} + \\
+ &e^{2az} + 2\sin(az \pm dx)\cos(ay \pm dz)e^{a(x+y)}]e^{-2d^2t}.
\end{aligned} \tag{67}
$$

Although the flow defined by these equations will probably never be physically realized, it has proven to be an excellent numerical benchmark [26].

A cube centered at $(0,0,0)$ and extending one unit in all three directions is discretized uniformly with 2 to 10 elements per edge. Using hexahedra this yields 8 to 1000 elements while with tetrahedra 48 to 6000 elements are used. The obvious ratio of 1:6 between hexahedra and tetrahedra occurs because the mesh generator for tetrahedra uses a hexahedral mesh as basis and then fills each hexahedron with 6 tetrahedra. Next, the Beltrami solutions (66) are imposed on the cubic surfaces as Dirichlet boundary conditions. The pressure (67) is defined in one central node per mesh. The constants $a = \frac{1}{4}\pi$ and $d = \frac{1}{2}\pi$ are chosen as proposed by Ethier and Steinman [26]. Tests are executed from $t_0 = 0$ stepping to $t_n = 0·1$ in 100 equal steps Δt using the Euler implicit discretization scheme. Numerical results at t_n are compared to the analytical solution using a normalized L_2 difference norm defined as

$$
\varepsilon_v = \max_k \frac{\| \underline{v}_k^h - \underline{v}_k \|_{L_2}}{\| \underline{v}_k \|_{L_2}}, \tag{68}
$$

where $\underline{v}$ is the column containing the velocity unknowns and $\| \cdot \|_{L_2}$ is the discrete L_2 norm defined by

$$
\| \underline{a} \|_{L_2} = \left(\sum_{i=1}^N a_i^2 \right)^{\frac{1}{2}}. \tag{69}
$$

The same difference norm can be used to determine the error of the pressure approximation, yielding ε_p. The errors ε_v and ε_p of the various computations as well as their CPU time and the number of degrees of freedom are stored. Figure 9 shows the errors ε_u and ε_p as functions of the nodal spacing and the number of degrees of freedom for both tetrahedra ($\triangle$) and hexahedra ($\square$).
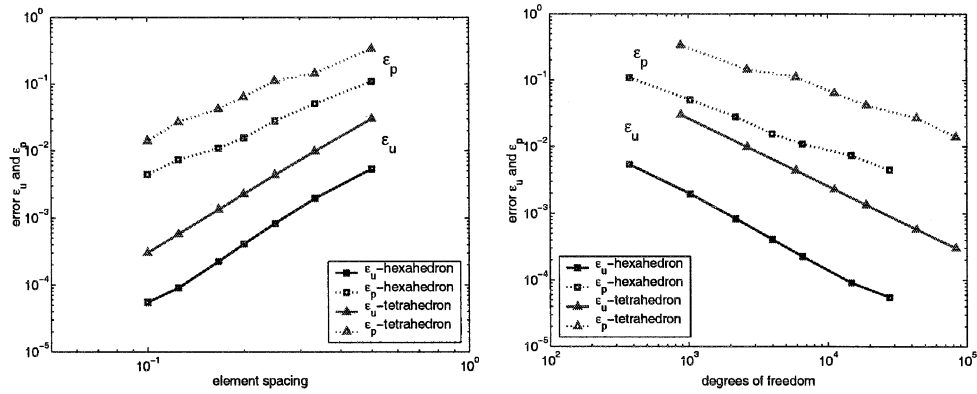
Figure 9. Errors ε_v and ε_p *vs.* nodal spacing (left) and *vs.* the number of degrees of freedom (right) obtained from the Beltrami test at $t_n = 0.1$ s.
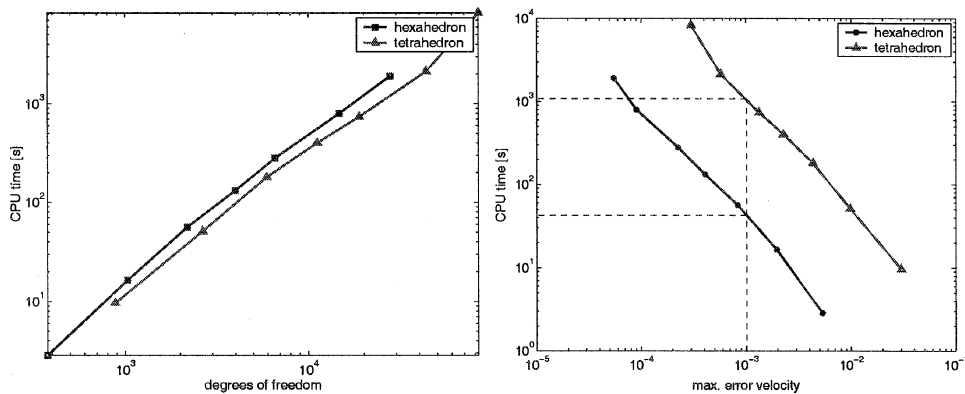

Figure 10. Logarithmic plot of the CPU-time needed for the computation to reach convergence for all time steps *vs.* the number of degrees of freedom (left) and error ε_v (right).

The slopes of the lines through the logarithmic data show a $O(h^3)$ performance of the velocity for both hexahedra and tetrahedra, while the pressure shows a $O(h^2)$ decay for both shapes. Figure 10 shows the relation between CPU-time and the accuracy of the computed velocity fields. It shows the actual efficiency of the 15-node tetrahedron ($\triangle$) in comparison to the efficiency of the 27-node hexahedron ($\square$).

The obvious drawback of using the tetrahedra can be illustrated by checking the extra CPU-time needed in comparison to the hexahedra when demanding a certain accuracy of computations. This drawback, however, is partially caused by the mesh generation. The performance of finite-elements is highly dependent on the acuteness of their angles and since the hexahedral meshes consisted of perfectly straight cubes, their results are somewhat idealized. The tetrahedral meshes, on the contrary, are made using a cubic grid, which results in less appropriate tetrahedra as one would have hoped. Some extra tests with less appropriate meshes similar to the one depicted in Figure 4.4 show that an increase in shear angle α leads to an immediate decay in accuracy when using hexahedra. Tetrahedral meshes on the other hand seem to increase their performance when the angle α remains below $30°$. This shows that the initial mesh (at $\alpha = 0°$) is not optimal for tetrahedra and results may improve when a better mesh generator is used.
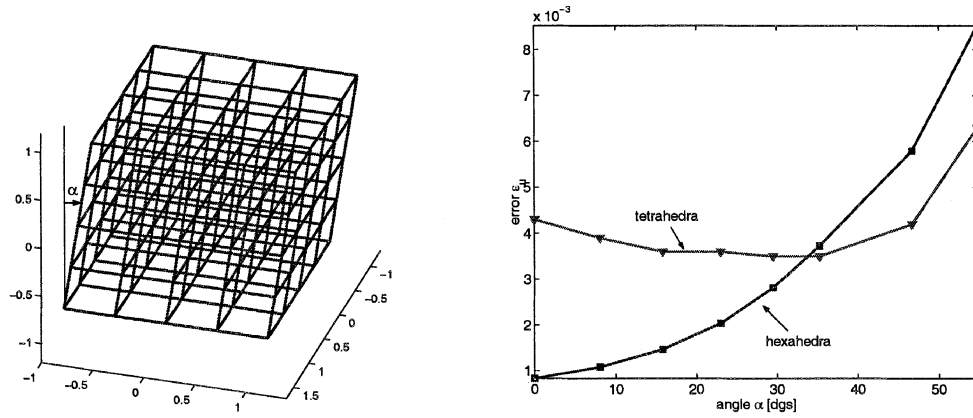
Figure 11.   Left: mesh of less appropriate hexahedra where α is the angle between the vertical edges of the straight cubic and the edges of the oblique one. *Right:* Plot of this angle *vs.* error ε_v in the Beltrami test for tetrahedra and hexahedra.
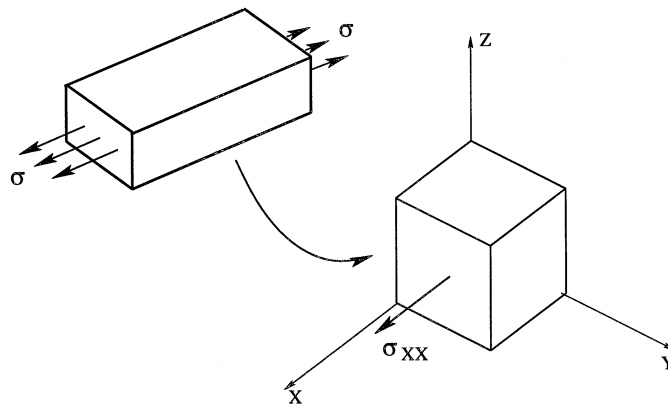

Figure 12.   Basic geometry for the uni-axial tensile test.

The precise relation between angle α and computational accuracy is not further examined here since only an indication of the idealized results of the hexahedra is needed. Since in the vascular domain sharp edges may be inevitable, the accuracy of the hexahedra will certainly be less favorable than the results of the Beltrami test speculate. However, when using an optimal tetrahedral mesh, their accuracy may even increase and become a good alternative for the hexahedron.

4.2.   SOLID DEFORMATION

In this section the performances of the extended quadratic tetrahedron for solid mechanics are discussed. Characteristic test problems are simulated in order to demonstrate the performance of the element. First an uni-axial tensile test will be simulated. After that a cantilever beam will be loaded at its free end to simulate pure bending. Finally a pipe segment will be inflated by means of an internal pressure. All test results will be compared to the results obtained by using the extensively tested 27-noded hexahedral element. Also, when an analytical solution is present this solution will be used for comparison as well.
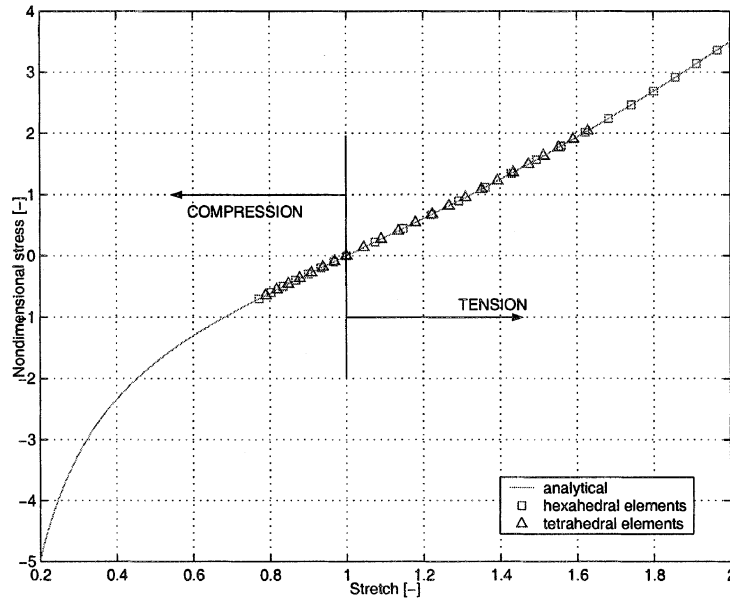
Figure 13. Non-dimensional stress $\sigma^* = \sigma_{xx}/G$ as a function of the stretch λ for the neo-Hookean model.

4.2.1. *Uni-axial tension*

A common way to model an uni-axial tensile or compression test is by using a unit-cube as depicted in Figure 12. The planes $x = 0$, $y = 0$ and $z = 0$ will be restrained in their normal directions. These Dirichlet boundary conditions ensure symmetry. Two types of applied boundary conditions on one of the remaining faces can be distinguished. Either essential boundary conditions can be prescribed or natural boundary conditions may be imposed to stretch the cube. The latter impose a stress on a surface, while the former prescribe displacements of a specific surface. To test the incompressibility assumption, Dirichlet boundary conditions are imposed. Prescribing the displacement in one direction should result in changing dimensions in the other two directions where no volume change may occur in the case of incompressible materials. In this uni-axial elongation of an incompressible material the Cauchy stress in the principle stretch direction can be expressed by $\sigma_{xx} = G(\lambda^2 - 1/\lambda)$.

First, a displacement normal to the yz-surface is applied to check to what extend the incompressibility constraint holds. Next the unit cube is loaded by a normal stress. The unit cube will be meshed with both hexahedral and tetrahedral elements. Both solutions are compared to the analytical solution.

Due to the nature of this experiment mesh refinement does not give any additional information other than more computational costs leading to the same results. Hence only two different meshes of the unit cube are used. One hexahedral mesh containing one 27-noded element and one tetrahedral mesh containing six 15-noded tetrahedral elements. The number of nodes in the meshes is, respectively, 27 and 51. In the hexahedral mesh the element has its ideal geometry. In order to test the influence of element distortion also a 'patch test' is performed. Eight irregular hexahedral elements were created in the cube, but the results are unaffected with respect to the regular hexahedra.

The tests with prescribed displacements show that no volume change occurs in either compression or tension. Stretches within the range of 0·6 to 4·0 are realized without a changing volume for hexahedral elements. For the tetrahedra a little less compression is possible and
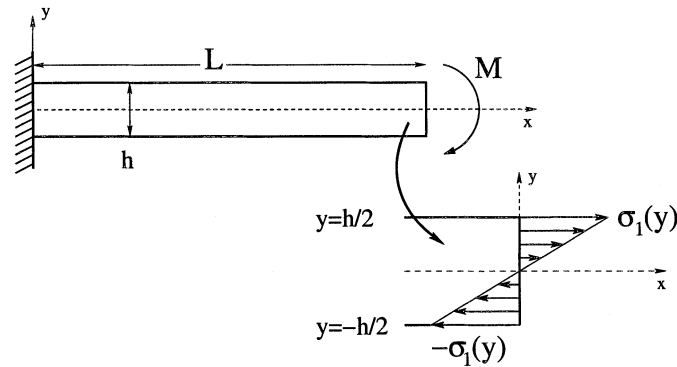
Figure 14. Cantilever beam loaded by a bending moment at its free end as seen from the positive z-direction. The free end is represented in more detail in the lower right corner.

in tension stretches of $\lambda = 2$ are feasible without resulting in distorted elements. Analytically there are almost no restrictions to the stretch λ. However, the tests with prescribed stresses show slightly different results. Although the volumes remain constant the stretch maxima are reduced. The hexahedral elements can sustain strains up to about 100% in tension, while tetrahedral elements can sustain as much as 60%. In compression both elements can reach a maximum of approximately 23%. In Figure 13 the results are displayed graphically. As can be seen, within their own range both hexahedral and tetrahedral elements describe the incompressible neo-Hookean model within the convergence criterion, which was set to 10^{-12}. The error in stretch between the analytical solution and the tetrahedral and analytical solution is of order 10^{-7}.

When the CPU-time of both simulations are compared, one can see that the CPU time per node is less for the tetrahedral than for the hexahedral element. But as a consequence of the larger number of nodes in the tetrahedral mesh, the overall computational costs are higher. A quantitative comparison will be given in the next section.

4.2.2. *Pure bending*

Besides the uni-axial tensile test to evaluate the element's performance, one can subject a test sample to a bending moment. Schematically such a test is depicted in Figure 14. A cantilever beam of length L is loaded at its free end by a distributed load $\sigma(y)$ as a function of the height of the beam at $x = L$. This will produce the desired bending moment M. If the length of the beam is substantially longer than the height and the width of the test sample, *i.e.*, at least a factor 10, elastic-beam theory can be applied. The deflection v of the beam in any point on the neutral surface ($\varepsilon_x = 0$) is the displacement of that point in the y-direction and can be computed by $v = \sigma_1 L^2 / Eh$ in which σ_1 is the maximal stress (see Figure 14). The Young's modulus E can be related to the shear modulus by $E = 2G(1+\nu)$. If incompressible materials are investigated, ν is equal to 0·5.

The beam dimensions are set to create a geometry of a length that equals 10 and a width and height of both 1. One end is completely restrained, while on the opposite end boundary elements are created to apply the distributed stress in the normal direction. Again, both hexahedral and tetrahedral elements are used to compare the results with the analytical solution. Only small deflections can be compared to this analytical solution.

The number of elements is varied in order to vary the discretization distance (length of an element). In Figure 15 the results of the errors as function of the discretization distance are
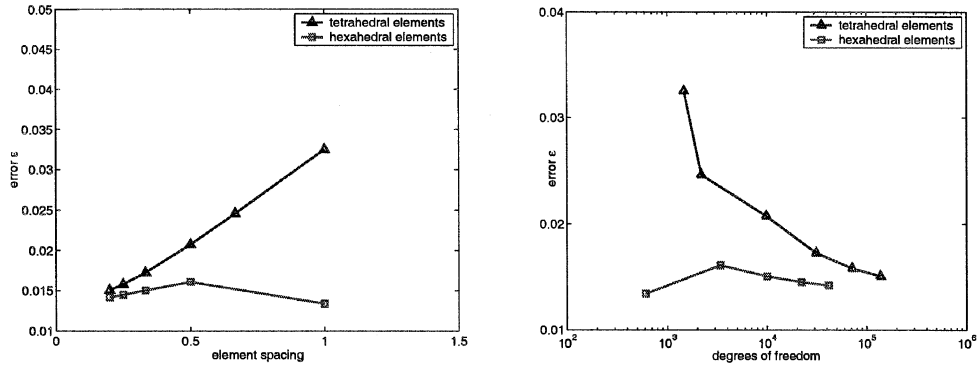
Figure 15. Results of the bending test for tetrahedral and hexahedral elements: The error as function of the discretization distance (left) and the error as function of the number of degrees of freedom (right).
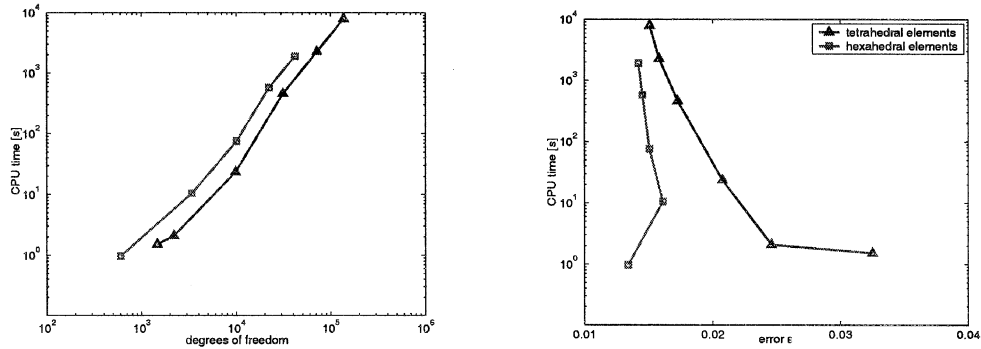

Figure 16. Results of the bending test for tetrahedral and hexahedral elements: The CPU-time as function of the number of degrees of freedom (left) and the error as function of the CPU-time (right).

depicted for both types of element shapes. The error is defined as:

$$\epsilon = \frac{|v^h - v|}{|v|}, \tag{70}$$

where v^h and v are, respectively, the numerical deflection computed and the analytical deflection and the analytical deflection $v = \sigma_1 L^2 / Eh$. Within practical limitations convergence to the analytical solution can be seen.

In Figure 16 the computational time as a function of the total number of degrees of freedom is plotted. It is observed that the CPU-time consumption is less for tetrahedral elements than for hexahedral elements with an equal number of degrees of freedom. Unfortunately this gain is relatively small. The right figure of Figure 16 displays the error as a function of the computational cost. To reach the same accuracy, tetrahedral elements consume a factor $O(3)$ more CPU-time than the hexahedra.
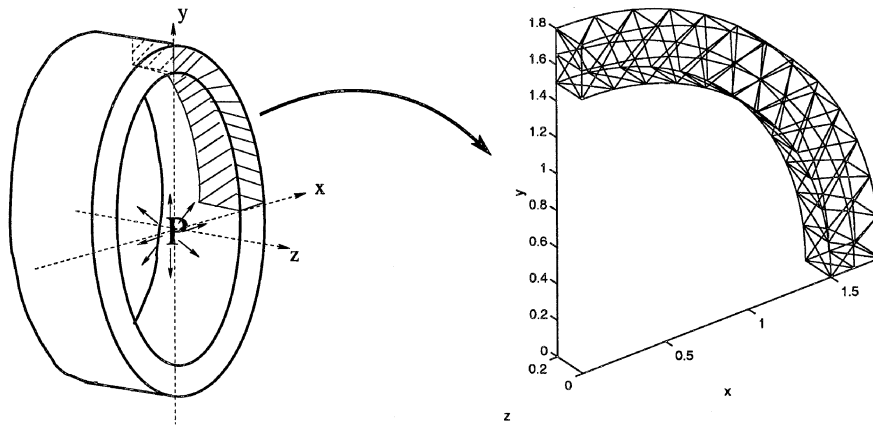
Figure 17. Thick-walled cylinder under internal pressure (left) and an example of a meshed geometry with tetrahedral elements (right).

5. Illustrative applications

5.1. DEFORMATION OF A THICK-WALLED TUBE

In this section the deformation of a thick-walled tube resulting from an internal pressure will be considered. For both an isotropic and an anisotropic tube wall material, the approximate solutions obtained with hexahedral and tetrahedral elements will be compared.

5.1.1. *Isotropic material*
A tube segment is inflated by means of an internal pressure. Because of the symmetrical nature of this problem only a quarter of the tube segment is used for the numerical analysis (see Figure 17). The segment will be loaded with an internal pressure p, which is varied in time. In one time period the pressure is increased sinusoidally from zero to a maximum pressure and back to zero again.

A comparison is made between hexahedral elements and tetrahedral elements. The radial displacements in both cases are compared as well as the radial stresses. In Figure 18 the radii are displayed as functions of the internal pressure. The differences between both element shapes are negligible, *i.e.*, the relative difference between the hexahedral and tetrahedral simulations with respect to the solution of hexahedra is of order $O(10^{-4})$. Increasing the number of elements yields a decrease in deviation with respect to the hexahedral solution.

In Figure 19 the non-dimensional radial stress is plotted for both element shapes. Both simulations result in similar stress distributions. Although the analytical solution of this problem is beyond the scope of this article, it is clear that at the inner and outer radius the boundary conditions are satisfied, *i.e.*, the stress at the inner radius is equal to $-p$, while at the outer surface the stress equals zero. Finally the simulations demonstrate a decrease in difference between the solutions of the tetrahedral and hexahedral elements when mesh refinement is applied.

5.1.2. *Composite material*
In the previously described tests isotropic materials are used. The incorporation of fibers is best demonstrated using a multi-layer constitutive model of arterial walls as proposed in Holzapfel [4]. The material properties of the layers (for both the matrix material and the fibers)
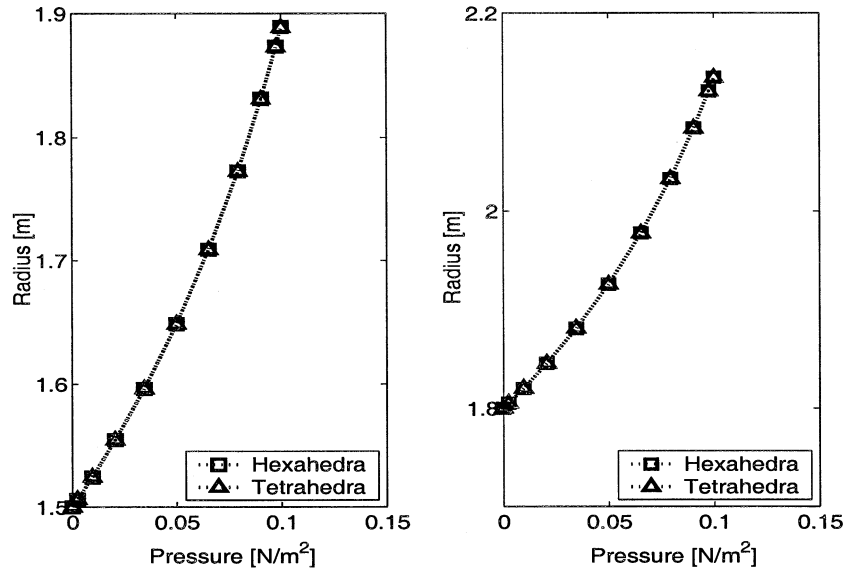
Figure 18. The difference between hexahedral and tetrahedral elements in inner (left) and outer radius (right) of a cylinder as a function of the internal pressure.
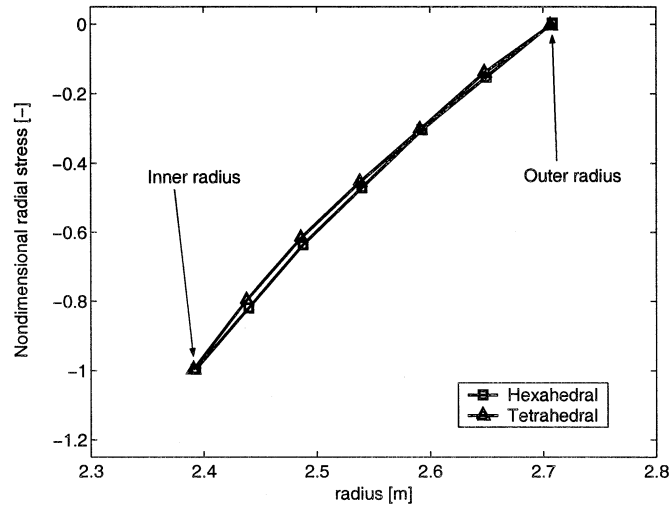

Figure 19. Non-dimensional radial stress $\sigma^* = \sigma_r / p$ over the wall thickness (Data obtained from simulations on $t = 0\cdot5$ [s] thus with internal pressure $p = 0\cdot2$ [N/m^2]).

are obtained from histological information of the rabbit carotid artery. For the constitutive equations for the media and adventitia this yields, respectively:

$$\boldsymbol{\sigma}_j = -p\mathbf{I} + \boldsymbol{\tau}_{m,j} + \sum_{i=1}^{2} \tau_{f,ij}\mathbf{e}_{ij}\mathbf{e}_{ij} \tag{71}$$

with

$$\boldsymbol{\tau}_{m,j} = G_{m,j}\,(\mathbf{B} - \mathbf{I}) \quad \text{and} \quad \tau_{f,ij} = 2k_{1j}\lambda_{ij}^2(\lambda_{ij}^2 - 1)\mathrm{e}^{k_{2j}(\lambda_{ij}^2 - 1)^2}. \tag{72}$$

Table 1. Material coefficients for rabbit carotid arteries.

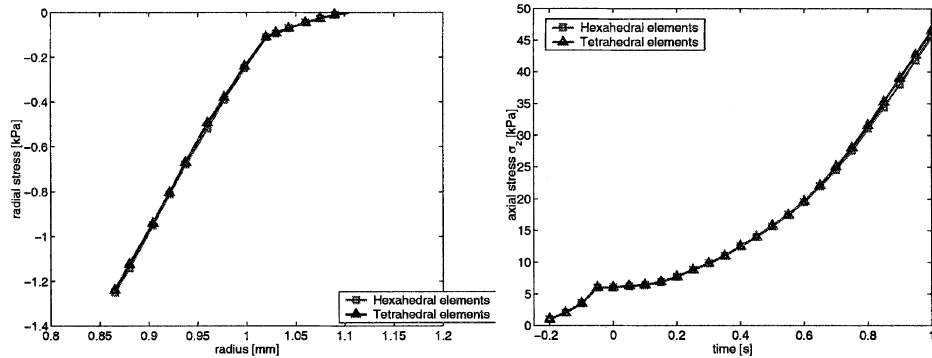|	G_m	k_1	k_2
Media	3·0 kPa	2·3632 kPa	0·8393
Adventitia	0·3 kPa	0·5620 kPa	0·7112

Figure 20. Radial stress in the artery as a function of the radius (left) and the axial stress as function of the time (right).

The index j distinguishes between the media and adventitia, whereas $G_{m,j}$, k_{1j} and k_{2j} are the material parameters as presented in Table 1. Finally $\mathbf{e}_{ij}$ denote the unit vectors of the two fiber directions in both layers.

In this test the artery is modeled as a straight circular vessel which contains residual stresses in the axial direction as well as in the circumferential direction before the vessel is pressurized. The internal pressure is increased quadratically in time to 20 kPa after 1 second.

The results of the FEM simulations with hexahedra and tetrahedra are pictured in Figure 20. As can be seen different finite-element shapes yield the same stress distributions. To display the differences in magnitude the radial stresses for both shapes are plotted *vs.* the radial position in the arterial wall (see Figure 20). The two different layers can be distinguished clearly.

The axial strain is zero since axial displacement is suppressed. As a result of this the stress in the axial direction increases with increasing radial displacement. In the right figure of Figure 20 the axial stresses are plotted as functions of time. Note that the 'negative' time is used to introduce the pre-stressed initial configuration. Once again the tetrahedral solution is compared to the hexahedral solution. The maximum difference of 2% between hexahedra and tetrahedra is found at the maximum pressure ($t = 1$ [s]).

5.2. FLOW IN A COMPLIANT CURVED TUBE (ALE)

As an illustration of the ALE method for problems where fluid flow and solid deformation are weakly coupled, in this section the flow of a non-Newtonian shear thinning fluid in a curved tube will be considered. The problem will be scaled to the situation in coronary arteries where the order of magnitude of the amplitude of the pressure waves amounts $O(10$ kPa$)$ whereas the flow-induced pressure differences ρV^2 are much smaller $O(0\cdot1$ kPa$)$.
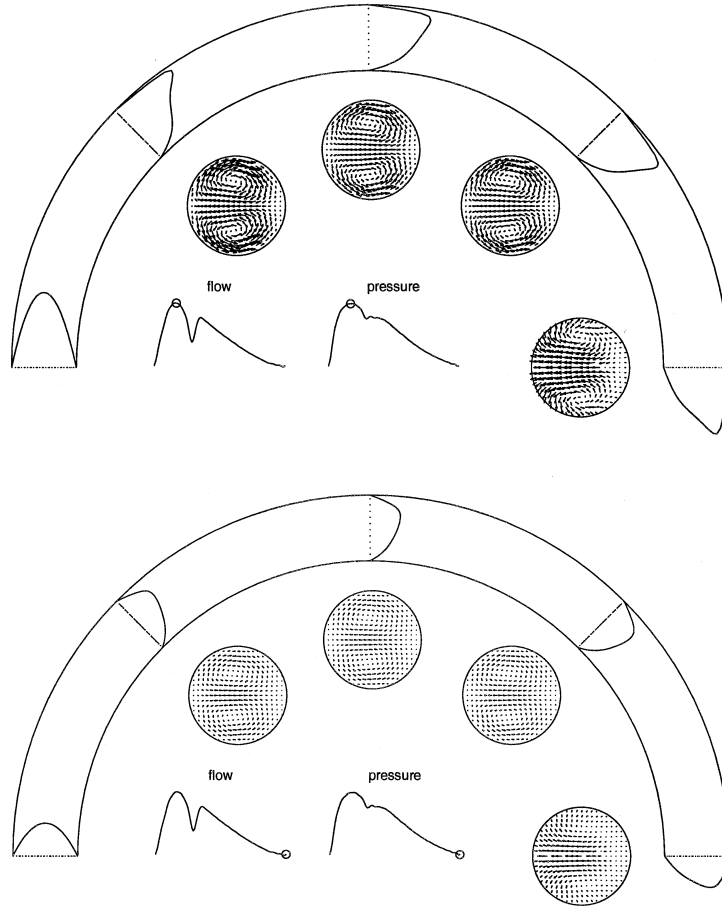
Figure 21. Axial and secondary velocity field of a Carreau-Yasuda fluid in four cross-sections of a rigid curved tube representing a right coronary artery at peak systolic (top) and end diastolic (bottom) phase of the cardiac cycle.

We consider a curved tube with radius $a = 1.5 \times 10^{-3}$ [m] and wall thickness $h = 1.5 \times 10^{-4}$ [m] and a radius of curvature of $R = 1.5 \times 10^{-2}$ [m]. Moreover, a neo-Hookean wall material with a shear modulus $G = 0.2$ [MPa] is assumed. The importance of the non-Newtonian properties of blood will not be shown in this study; for this the reader is referred to Gijsen *et al.* [2, 3]. The fluid inside the tube is assumed to be a generalized Newtonian fluid that can be described by the Carreau-Yasuda model (8). The parameters of the model are chosen such that the viscous behavior mimics that of blood [2, 3], *i.e.*, $\rho = 1080$ [kg/m^3], $\eta_0 = 5.19 \times 10^{-2}$ [Pa s], $\eta_\infty = 4.76 \times 10^{-3}$ [Pa s], $a = 4.09 \times 10^{-1}$ [–], $n = 1.91 \times 10^{-1}$ [–] and $\lambda = 4.38 \times 10^{-1}$ [s]. Pressure and flow curves are adopted from [27, Chapter 10]. Based on the mean flow of 100 ml/min, a Reynolds number can be defined with respect to the viscosity at high shear η_∞ and is in the order of 150. A cardiac time period of $T = 0.75$ [s] is taken, yielding a Womersley-number equal to 2.4.

The approximate solutions of two periods of 128 time steps per period are computed. The results shown are for the second period. For each time step the wall motion is computed using the pressure curve as depicted in the Figures 21 and 22. The movement of one node at the outer wall of the in-stream has been suppressed in all directions. Both the wall motion and a
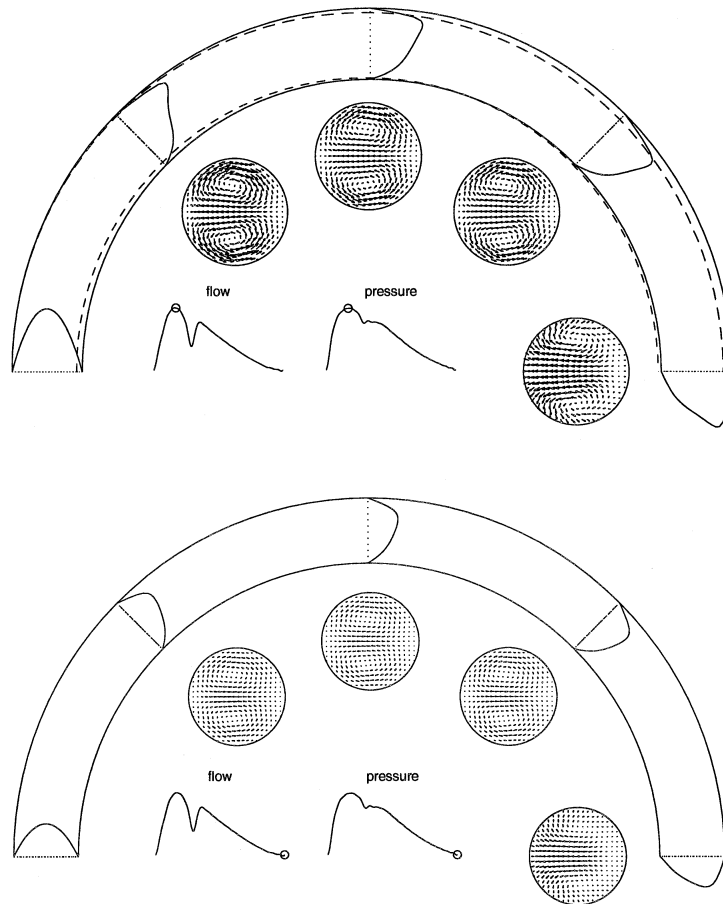
Figure 22. Axial and secondary velocity field of a Carreau-Yasuda fluid in four cross-sections of a compliant curved tube representing a right coronary artery at peak systolic (top) and end diastolic (bottom) phase of the cardiac cycle. The dotted lines represent the geometry at diastolic pressure.

parabolic in-stream profile based on the flow curve given in the figure are used as boundary conditions for the fluid problem. At the outflow a traction-free condition is used.

The results show that the velocity profiles and thereby the wall shear stress in the rigid curved tube differs considerably from the one in the compliant tube, although the main flow characteristics are equal.

5.3. HYDRODYNAMIC INTERACTION OF TWO VALVES (FD)

The fictitious-domain method will be illustrated by means of a simulation of pulsating flow in a 2D cavity with two valves. This configuration can be seen as a simplified model of the flow in the left ventricle. The width of the inflow (right top) and outflow (left top) channel is assumed to be H (see Figure 23). The radius of curvature of the bifurcation point is $0.2H$ so the total width of the cavity is $2.4H$. At inflow boundary at the bottom of the cavity (not shown in Figure 23) a sinusoidal plug flow in time $U = U_0 \cos \omega t$ is prescribed. The constant viscosity and density are taken such that during peak flow the Reynolds number based on the width of the in- and outflow channels amounts to 2400. The Strouhal number for this configuration is 0.042. The constant pressure at the outflow boundary (left) is five times higher than the

pressure at the inflow (right). So the system works as a pump pumping fluid from a low to a high pressure.

With respect to the fluid flow, the two valves are assumed to be thin and only at the downstream side of the valve a fictitious-domain coupling is made. In this way an over-constrained coupling is circumvented. The rotation points of the valves are clear from Figure 23.

Straightforward application of the fictitious domain procedure as prescribed in Section 2.5 for this configuration will not result in a realistic and stable solution. There are two reasons for this. First, when the valves are closed and have to carry a significant pressure, leakage through the valves will occur because of the linear pressure approximation in the fluid elements that are cut by the valve. Secondly, the vorticity generated by the moving valves in the in- and outflow channels will interact with the boundary condition and yield an unstable flow. The latter problem is specific for the configuration chosen. It can either be solved by moving the outflow boundaries far away from the valves or by introducing an artificial viscosity in the channel when the valve is closed. The second solution is selected in this study. The first problem, however, is generic and known from earlier studies [19]. For rigid valves, the following solution is proposed. The initial fluid mesh is such that boundaries Γ_{fd} of the valves in closed position coincide with boundaries of elements Ω_f^e in the fluid domain Ω_f. In this way large pressure differences over the valves can be sustained without leakage due to the fact that in the Crouzeix-Raviart elements the pressure is discontinuous over the element boundaries. As the valves in closed position may deform slightly due to the pressure forces, the valve is kept in its initial closed position as long as the pressure force is not in the direction that would open the valve.

The results of the simulation are summarized in Figure 23 where the velocity fields at six successive instants of time during one (the second) flow cycle are given. The low-pressure valve (right) closes in a time period after maximum flow acceleration during which a significant retrograde flow (regurgitation) is present. Once the low-pressure valve is closed, forward flow in the high-pressure valve is found until a moment of time shortly after maximum deceleration. The regurgitation through the high-pressure valve is much less than through the low-pressure valve. A thorough analysis of the valve dynamics is beyond the scope of this paper and needs a series of simulations in which the Reynolds and Strouhal number are varied. The results shown do indicate, however, that such an analysis can be very well performed using the fictitious-domain method as presented in this paper.

6. Conclusions and discussion

In this paper a finite-element-based method for cardiovascular fluid-structure interaction problems has been presented. The method proposed in this paper is based on an arbitrary Lagrange-Euler method combined with a fictitious-domain approach. This combined (ALE-FD) method is based on standard finite-element approximations for fluid flow and solid deformation and by virtue of this can be used for most constitutive models for the fluid and the solid. In this study, an inelastic generalized Newtonian fluid [2, 3] and a fiber-reinforced solid [22] is chosen and thereby typical non-Newtonian behavior of blood and nonlinear behavior of vascular tissue can be described.

The linearized finite-element equations have been derived and described, including the linearization process to deal with constitutive and geometrical nonlinearities and the incorporation of boundary conditions and coupling between fluid and solid domains. The linearized
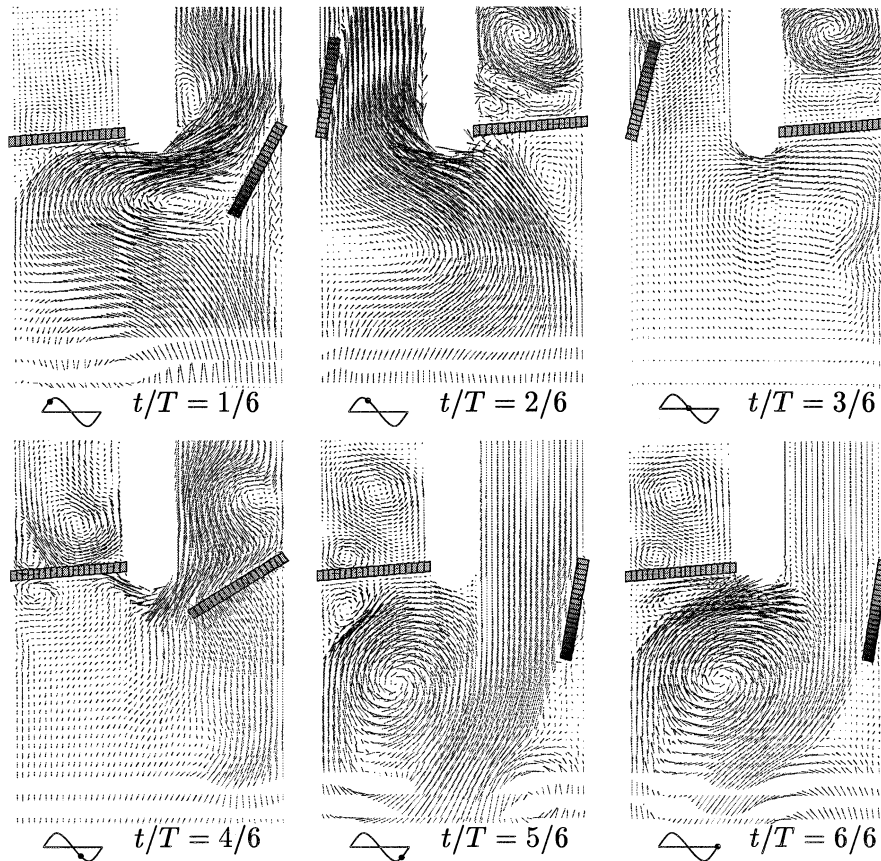
Figure 23. Valve dynamics during six successive instants of time in one cycle of an imposed flow pulse.

systems for fluid flow, solid deformation and fluid-structure interaction are solved using a special renumbering of degrees of freedom and an incomplete ILU preconditioned BiCGStab iterative solver [25]. Even though convergence of the system is achieved in the problems considered in this paper, it needs further investigation to decide whether or not this solution method is optimal.

Special attention has been paid to the choice of elements that are suitable for the ALE-FD method. Linear elements are known to be quite inaccurate both for fluid flow and solid deformation and are not considered in this study. However, the efficiency that can be achieved with these elements would justify further investigation [28]. Due to the requirement of fictitious-domain methods that are used for thin solid structures that can bear significant pressure forces, fluid and structure elements with a continuous pressure approximation are ignored in this study. Consequently, only the quadratic tetrahedral ($P_2^+ P_1$) and hexahedral ($Q_2^+ P_1$) Crouzeix-Raviart elements have been considered.

For approximate solutions of the Navier-Stokes equations we found a similar convergence for tetrahedral and hexahedral elements using an exact Beltrami flow solution. Hexahedral elements seem to be advantages with respect to accuracy but an experiment with a skewed mesh showed that, once the mesh is distorted, tetrahedral elements may give comparable or even better results. A more detailed study with different kinds of meshes for complex domains is needed in order to be more conclusive in this respect.

The performance of the tetrahedral elements for solid deformation has been investigated by means of three characteristic tests, uni-axial tension, pure bending and deformation of a tube. All these tests show no significant difference between the solutions obtained with hexahedral and tetrahedral elements, although the hexahedral elements are definitely more accurate for the cases studied in this paper. When looking at the computational costs, the tetrahedral elements are more efficient in terms of CPU-time per degree of freedom (DOF). But this advantage is not completely utilized, since more elements (DOFs) are needed to end up at the same accuracy as for hexahedral elements. Thus, even though the tetrahedra is faster per node, the overall cost to reach an arbitrary accuracy is still higher for tetrahedra. Obviously, since numerous elements for tetrahedral meshes can not be avoided, the efficiency can only be improved by reducing the computational costs per element.

Overall within the meshing flexibility of the mesh generators used, the performances of the Crouzeix-Raviart tetrahedron can not compete with the tri-quadratic hexahedron when it involves accuracy aspects *vs.* computational time. In the test problems all geometries are simple and, as a result of that, the meshes show 'ideal' hexahedral elements. A fairer comparison could probably be made with more irregular geometries. In this case the tetrahedron is expected to be favorable as regards mesh generation and probably with respect to efficiency as well. A final remark can be made about the costs of the tetrahedral element. A reduction in CPU-time per element would allow the use of more elements. Then, the tetrahedron can be more competitive than the hexahedron in terms of cost efficiency. In two-dimensional problems this is achieved by elimination of degrees of freedom in the centroidal node of a Crouzeix-Raviart triangle. A three-dimensional analogue of this modified Crouzeix-Raviart triangle would probably be worthwhile investigating.

The incorporation of fibers in isotropic matrix material is demonstrated to be straightforward. Instead of just defining a shear and a bulk modulus (in the case of compressible solids), one also needs to specify the fiber-material properties. The executed simulations were not a profound analysis but more a leg-up regarding the applicability in biomechanical surroundings.

The results obtained for the curved-tube flow show that the velocity profiles and thereby the wall shear stress in the rigid curved tube considerably differ from the one in the compliant tube. The ALE method can certainly be used to investigate the importance of this difference with respect, to for instance, wall shear stress, an important parameter with respect to the development of atherosclerosis or aneurysms and restenosis after balloon-angioplasty with or without stent procedure.

Finally, the potential of a combined arbitrary Lagrange-Euler fictitious-domain method (ALE-FD) has been demonstrated for a simplified model of the left ventricle with rigid (mechanical) valves. A special procedure has been proposed to achieve that the fictitious-domain approach is able to describe thin structures that may sustain relatively large pressure forces. In that case the fictitious-domain boundary must coincide with boundaries of the fluid-domain elements. Extension of this procedure for non-rigid solid structures by means of local remeshing of the fluid domain is currently under investigation.

References

1. C.A. Taylor, Predictive medicine: computational techniques in therapeutic decision-making. *Computer Aided Surgery* 4 (1999) 231–247.

2.   F.J.H. Gijsen, E. Allanic, F.N. van de Vosse and J. D. Janssen, The influence of the non-Newtonian properties of blood on the flow in large arteries: unsteady flow in a 90° curved tube, *J. Biomech.* 32 (1999) 705–713.

3.   F.J.H. Gijsen, F.N. van de Vosse and J.D. Janssen, The influence of the non-Newtonian properties of blood on the flow in large arteries: steady flow in a carotid bifurcation model. *J. Biomech.* 32 (1999) 601–608.

4.   G.A. Holzapfel, A new constitutive framework for arterial wall mechanics and a comparative study of material models. *Elasticity* 61 (2000) 1–48.

5.   M. Fortin, Old and new finite-elements for incompressible flow. *Int. J. Num. Meth. Fluids* 1 (1981) 347–354.

6.   M.P. Robichaud and P.A. Tanguy, Comparison of 3-D finite-elements for fluid flow. *Commun. Appl. Num. Meth.* 22 (1987) 1251–1267.

7.   J. Donea, S. Giuliani and J.P. Halleux, An arbitrary Langragian-Eulerian finite-element method for transient dynamic fluid structure interactions. *Comp. Meth. Appl. Mech. Engng.* 33 (1982) 689–723.

8.   P.J.G. Schreurs, *Numerical Simulation of Forming Processes: the use of the Arbitrary-Eulerian-Langrangian (AEL) Formulation and the Finite Element Method.* PhD thesis, University of Technology, Eindhoven (1983) 136 pp.

9.   A.A. Johnson and T.E. Tezduyar, Mesh update strategies in parallel finite element computations of flow problems with moving boundaries and interfaces. *Comp. Meth. Appl. Mech. Engng.* 119 (1994) 73–94.

10.   P.J.R. Reuderink, *Analysis of the Flow in a 3D Distendible Model of the Carotid Artery Bifurcation.* PhD thesis, University of Technology, Eindhoven (1991) 138 pp.

11.   K. Perktold and G. Rappitsch, Computer simulation of local blood flow and vessel mechanics in a compliant carotid artery bifurcation model. *J. Biomech.* 28 (1995) 845–856.

12.   M.C.M. Rutten, *Fluid Solid Interaction in Large Arteries.* PhD thesis, University of Technology, Eindhoven (1998) 124 pp.

13.   F. Bertrand, P.A. Tanguy and F. Thibault, A three-dimensional ficticious domain method for incompressible flow problems. *Int. J. Num. Meth. Fluids* 25 (1997) 719–736.

14.   R. Glowinski, T.W. Pan and J. Periaux, Distributed Lagrange multiplier methods for incompressible viscous flow around moving rigid bodies. *Comp. Meth. Appl. Mech. Engng.* 151 (1998) 181–194.

15.   N.A. Patankar, P. singh, D.D. Joseph, R. Glowinski and T.-W. Pan, A new formulation of the distributed Lagrange multiplier/ficticious domain method for particulate flows. *Int. J. Multiphase Flows* 26 (2000) 1509–1524.

16.   C.S. Peskin and D.M. McQueen, A general method for the computer simulation of biological systems interacting with fluids. *Symposia Soc. Experimantal Biology* 49 (1995) 265–276.

17.   F.P.T. Baaijens, A fictitious domain/mortar element method for fluid-structure interaction. *Int. J. Num. Meth. Fluids* 35 (2001) 743–761.

18.   J. de Hart, G.W.M. Peters, P.J.G. Schreurs and F.P.T. Baaijens, A two-dimensional fluid-structure interaction model of the aortic valve. *J. Biomech.* 33 (2000) 1079–1088.

19.   J. de Hart, *Fluid-Structure Interaction in the Aortic Heart Valve: A Three-Dimensional Computational Analysis.* PhD thesis, University of Technology, Eindhoven (2002) 127 pp.

20.   R. Temam, *Navier-Stokes Equations.* Amsterdam: North-Holland (1977) 526 pp.

21.   J.D. Humphrey, Mechanics of the arterial wall: review and directions. *Crit. Rev. Biomed. Engng.* 23 (1995) 1–162.

22.   C.H.G.A. Oijen, *Mechanics and Design of Fibre Reinforced Vascular Prosthesis.* PhD thesis, University of Technology, Eindhoven (2003) 89 pp.

23.   R. Glowinski, T.W. Pan and J. Periaux, A Lagrange multiplier/fictitious domain method for the numerical simulation of incompressible viscous flow around moving rigid bidies: (i) case where the rigid body motions are known a priori. *C.R. Acad. Sci. Paris* 25 (1997) 361–369.

24.   F. Brezzi and M. Fortin, *Mixed and Hybrid Finite Element Methods.* New York: Springer-Verlag (1981) 350 pp.

25.   A. Segal, *SEPRAN Manual.* Leidschendam (Netherlands): Ingenieursbureau SEPRA (2000).

26.   C.R. Ethier and D.A. Steinman, Exact fully 3D Navier-Stokes solutions for benchmarking. *Int. J. Num. Meth. Fluids* 19 (1994) 369–375.

27.   R.M. Berne and M.N. Levy, *Cardiovascular Physiology.* St. Louis: Mosby (1967) 312 pp.

28.   F. Bertrand, M.R. Gadbois and P.A. Tanguy, Tetrahedral elements for fluid flow. *Int. J. Num. Meth. Engng.* 33 (1992) 1251–1267.